A STRICT TEST OF STELLAR EVOLUTION MODELS: THE ABSOLUTE DIMENSIONS OF THE MASSIVE BENCHMARK ECLIPSING BINARY V578 MON

E. V. Garcia[1,2,8], Keivan G. Stassun[1,3], K. Pavlovski[4], H. Hensberge[5], Y. Gómez Maqueo Chew[6], and A. Claret[7]

[1] Department of Physics and Astronomy, Vanderbilt University, 6301 Stevenson Center, VU Station B 1807, Nashville, TN 37235, USA; eugenio.v.garcia@gmail.com
[2] Lowell Observatory, Flagstaff, AZ 86001, USA
[3] Department of Physics, Fisk University, 1000 17th Avenue North, Nashville, TN 37208, USA
[4] Department of Physics, University of Zagreb, Bijenicka cesta 32, 10000 Zagreb, Croatia
[5] Royal Observatory of Belgium, Ringlaan 3, B-1180 Brussels, Belgium
[6] Physics Department, University of Warwick, Gibbet Hill Road, Coventry CV4 7AL, UK
[7] Instituto de Astrofsica de Andaluca, CSIC, Apartado 3004, E-18080 Granada, Spain

ABSTRACT

We determine the absolute dimensions of the eclipsing binary V578 Mon, a detached system of two early B-type stars (B0V + B1V, $P = 2.40848$ days) in the star-forming region NGC 2244 of the Rosette Nebula. From the light curve analysis of 40 yr of photometry and the analysis of HERMES spectra, we find radii of $5.41 \pm 0.04\,R_\odot$ and $4.29 \pm 0.05\,R_\odot$, and temperatures of $30{,}000 \pm 500\,K$ and $25{,}750 \pm 435\,K$, respectively. We find that our disentangled component spectra for V578 Mon agree well with previous spectral disentangling from the literature. We also reconfirm the previous spectroscopic orbit of V578 Mon finding that masses of $14.54 \pm 0.08\,M_\odot$ and $10.29 \pm 0.06\,M_\odot$ are fully compatible with the new analysis. We compare the absolute dimensions to the rotating models of the Geneva and Utrecht groups and the models of the Granada group. We find that all three sets of models marginally reproduce the absolute dimensions of both stars with a common age within the uncertainty for gravity-effective temperature isochrones. However, there are some apparent age discrepancies for the corresponding mass–radius isochrones. Models with larger convective overshoot, >0.35, worked best. Combined with our previously determined apsidal motion of $0.07089^{+0.00021}_{-0.00013}$ deg cycle^{-1}, we compute the internal structure constants (tidal Love number) for the Newtonian and general relativistic contribution to the apsidal motion as $\log k_2 = -1.975 \pm 0.017$ and $\log k_2 = -3.412 \pm 0.018$, respectively. We find the relativistic contribution to the apsidal motion to be small, $<4\%$. We find that the prediction of $\log k_{2,\mathrm{theo}} = -2.005 \pm 0.025$ of the Granada models fully agrees with our observed $\log k_2$.

Key words: binaries: close – binaries: eclipsing – stars: early-type – stars: individual (V578 Mon) – stars: massive

Online-only material: color figures, supplemental data

1. INTRODUCTION

Detached eclipsing binary stars (dEBs) provide accurate observed stellar masses, radii, effective temperatures, and rotational velocities. See a recent review by Torres et al. (2010) for a discussion of 94 dEBs with accurate masses and radii used to test stellar evolution models. There are only 9 total massive dEBs, or equivalently, 18 stars whose physical parameters have been determined with an accuracy of better than 3%, making V578 Mon 1 of only 9 EBs with $M_1 \geqslant M_2 > 10\,M_\odot$ and with sufficient accuracy to be included in the Torres et al. (2010) compilation of benchmark-grade EBs. Figure 1 demonstrates the upper main sequence (MS) of all dEBs with $M_1 \geqslant M_2 > 10\,M_\odot$ and masses and radii determined to 3% (adapted from Torres et al. 2010). V578 Mon is therefore a benchmark system for testing stellar evolution models of newly formed massive stars. The accurate absolute dimensions of eclipsing binary stars provide a unique opportunity to test stellar evolution models in two ways: using the isochrone test and using the apsidal motion test.

The isochrone test of stellar evolution models requires that the ages of both components of a dEB predicted from separate stellar evolution tracks be the same within the uncertainty of the absolute dimensions (M, R, $T_{\rm eff}$, $v_{\rm rot}$). For the isochrone test,

we assume that both components of the dEB formed together in the same initial gas cloud. Therefore, both components of a dEB are assumed to arrive at the zero age main sequence (ZAMS) at nearly the same time. Furthermore, their initial chemical compositions must be the same. Finally, we assume that each component of the binary evolves in isolation, where the effects of the companion star on the evolution is small or negligible.

The isochrone test is strongest for eclipsing binaries with low mass ratios $q = (M_2/M_1) < 1$. For dEBs where component masses $M_1 \approx M_2$, both stars will evolve on the same evolutionary track. This does not allow for strict tests of stellar evolution models unless the chemical composition or effective temperature of the stars is known. Stellar evolution models will predict that two stars of the same mass and composition will have the same age. Conversely, the larger the difference in initial mass between the components of the binary star, the larger the difference in MS lifetimes of the two stars. Therefore, stellar models must have accurate input physics to correctly predict how quickly stars of different masses evolve relative to each other. The correct input physics in turn yield correct predictions of the observed absolute dimensions of the detached eclipsing binary.

dEBs with apsidal motion (precession of the argument of periastron) also allow for the apsidal motion test of the stellar internal structure (Claret & Giménez 2010). Physically, the observed apsidal motion rate in an eclipsing binary is a result
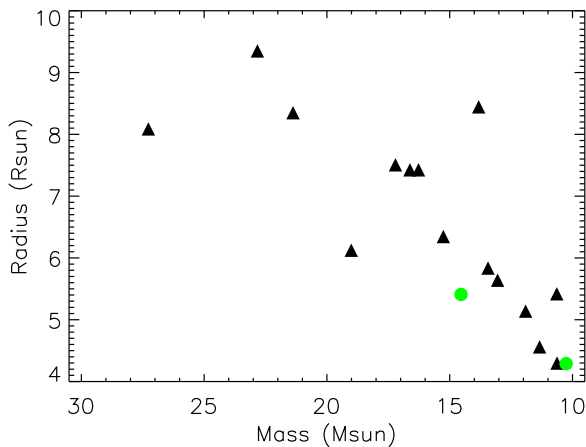
Figure 1. Massive ($>10\ M_\odot$) detached eclipsing binaries with accurate masses and radii better than 2% are scarce. There are only nine such systems (black triangles) including V578 Mon (green circles). This list of eclipsing binaries is adapted from Torres et al. (2010). The error bars on the mass and radii are smaller than the plotted symbols. Of these eclipsing binaries, V578 Mon is simultaneously one of the youngest and has one of the lowest mass ratios $q = M_2/M_1$.

(A color version of this figure is available in the online journal.)

of the tidal forces of each star on the other. In turn, this tidal force is linked to the internal structure of each star, the star's separation, their mass ratio q, and their radii R_1 and R_2. The internal structure is quantified by the constant $\log k_2$, which is the logarithm of twice the tidal Love number (Kramm et al. 2011). The apsidal motion test compares the theoretical internal structure constant $\log k_{2,\mathrm{theo}}$ to the observed internal structure constant $\log k_{2,\mathrm{obs}}$. The observed internal structure constant is a function of the observed absolute dimensions and apsidal motion of the eclipsing binary. The observed internal structure constant is very sensitive to the radii ($k_{2,\mathrm{obs}} \propto R^5$); therefore, this test can only be performed with accurate stellar radii. However, including this study of massive dEB V578 Mon, there are only five massive, eccentric eclipsing binaries available for these tests of internal structure (Claret & Giménez 2010).

Here we combine the previous determination of $\dot{\omega}$ and e from Garcia et al. (2011) with a re-analysis of 40 yr worth of photometry to re-determine the fundamental properties of V578 Mon. We also include the photometry used in the previous light curve analysis (Hensberge et al. 2000). We compare the masses, temperatures, and radii of V578 Mon with rotating high mass stellar evolution models by the Granada (Claret 2004, 2006), Geneva (Georgy et al. 2013; Ekström et al. 2012), and Utrecht (Brott et al. 2011) groups. We also compare the observed internal structure constant $\log k_{2,\mathrm{obs}}$ with theoretical $\log k_{2,\mathrm{theo}}$ using the methods of Claret & Giménez (2010).

2. THE ECLIPSING BINARY V578 MON IN NGC 2244

The photometric variability of the bright ($V = 8.5$), 2.408 day period, eccentric, massive dEB V578 Mon (HDE 259135, BD+4°1299), comprising a B1V-type primary star and a B2V-type secondary star was first identified in the study by Heiser (1977) of NGC 2244 within the Rosette Nebula (NGC 2237, NGC 2246). The identifications, locations, and photometric parameters for V578 Mon are listed in Table 1. The absolute dimensions of V578 Mon have been determined from three seasons of Strömgren *uvby* photometry and one season of radial-velocity data by Hensberge et al. (2000). An analysis of the metallicity and evolutionary status of V578 Mon was undertaken

Table 1
Identifications, Location, and Combined Photometric Parameters
for Eclipsing Binary V578 Mon

	V578 Mon	Reference
Henry Draper number	HD 259135	Cannon & Pickering (1923)
Bonner Durchmusterung	BD +04°1299	Argelander (1903)
Hoag number	NGC 2244 200	Hog et al. (1998)
α_{2000}	06 32 00.6098	Hog et al. (1998)
δ_{2000}	+04 52 40.902	Hog et al. (1998)
Spectral type	B0V + B1V	Hensberge et al. (2000)
V	8.542	Ogura & Ishida (1981)
$V - I$	0.262	Wang et al. (2008)
$B - V$	+0.165	Ogura & Ishida (1981)
$U - B$	-0.727	Wolff et al. (2007)
$V - R$	+0.452	Wang et al. (2008)

by Pavlovski & Hensberge (2005) and Hensberge et al. (2000). The masses and radii of V578 Mon determined from these data are $14.54 \pm 0.08\ M_\odot$ and $10.29 \pm 0.06\ M_\odot$, and $5.23 \pm 0.06\ R_\odot$ and $4.32 \pm 0.07\ R_\odot$ for the primary and secondary, respectively (Hensberge et al. 2000). V578 Mon was included in the list of 94 detached eclipsing binaries with masses and radii accurate to 2% by Torres et al. (2010). The radii for V578 Mon listed in Torres et al. (2010) were found to be incorrect by Garcia et al. (2013) given the system's eccentric orbit and asynchronous rotation. The apsidal motion $\dot{\omega}$ and a new eccentricity e were determined in Garcia et al. (2011). V578 Mon was observed by MOST (Pribulla et al. 2010).

Given the inclination of V578 Mon, its eclipses are partial, meaning that neither star is fully out of view of Earth. Partial eclipses can translate into a degeneracy between the radii, preventing the component radii R_1 and R_2 from being individually measured. However, V578 Mon also has an eccentric orbit, meaning that the eclipse durations are not equal, which helps break this degeneracy and allows the radii to be determined separately. V578 Mon is observed to have not yet tidally locked. The system has a low mass ratio $q = 0.7078$ compared with similar systems with well-determined absolute parameters such as V1034 Sco, V478 Cyg, AH Cep, V453 Cyg, and CW Cep (Bouzid et al. 2005; Popper & Etzel 1981; Popper & Hill 1991; Bell et al. 1986; Holmgren et al. 1990; Southworth et al. 2004; Popper 1974; Stickland et al. 1992). Of all of these systems, V578 Mon is also the youngest, making this system a benchmark case for testing stellar evolution models at the youngest ages.

3. DATA

3.1. Johnson UBV and Strömgren uvby Photometry

The available time series photometry of V578 Mon covers nearly 40 yr and more than one full apsidal motion period. A summary of the various light curve epochs, including filters and observing facilities used, is presented in Table 2. Photometry from Heiser (2010) includes multi-band light curves spanning 1967–2006 from the 16 inch telescope at Kitt Peak National Observatory (KPNO) and from the Tennessee State University (TSU)–Vanderbilt 16 inch Automatic Photoelectric Telescope (APT) at Fairborn Observatory. The KPNO Johnson *UBV* light curves comprise 725 data points spanning 1967–1984 with average uncertainties per data point of 0.004 mag computed by Heiser (2010). The APT Johnson *BV* light curves span 1994–2006 and consist of 1783 data points with average

Table 2
V578 Mon Light Curves

Observatory	Year	Filter	σ_0 (mag)	σ (mag)	N
KPNO[a]	1967–1984	Johnson U	0.004	0.016	251
		Johnson B	0.004	0.012	256
		Johnson V	0.004	0.013	217
SAT[b]	1991–1994	Strömgren u	0.0029	0.0067	248
		Strömgren b	0.0023	0.0046	248
		Strömgren v	0.0023	0.0054	248
		Strömgren y	0.0030	0.0053	248
APT[c]	1994–1995	Johnson V	0.0037	0.0022	260
		Johnson B	0.001	0.0040	254
APT	1995–1996	Johnson V	0.002	0.0035	95
		Johnson B	0.001	0.0037	96
APT	1999–2000	Johnson V	0.002	0.0058	259
		Johnson B	0.001	0.0078	246
APT	2005–2006	Johnson V	0.002	0.0036	284
		Johnson B	0.001	0.0044	283

Notes.
[a] 16 inch telescope at Kitt Peak (KPNO).
[b] 0.5 m telescope at La Silla (SAT).
[c] TSU–Vanderbilt 16 inch telescope at Fairborn University (APT).

uncertainties per data point of 0.001 mag for *B* and 0.002 mag for *V* (Heiser 2010). Light curves from Hensberge et al. (2000) span 1991–1994 from the 0.5-m Strömgren Automatic Telescope (SAT) at La Silla, with 248 data points in each of the *uvby* filters and average uncertainty per data point of 0.003 mag (Hensberge et al. 2000). We begin our light curve analysis with the observational errors originally estimated by Heiser (2010) and Hensberge et al. (2000). Table 2 lists these average uncertainties, σ_0, as reported by the original authors. However, from our light curve fits (see below) we found that these uncertainties were in most cases underestimated. Thus, we also report as σ in Table 2 the uncertainties that we ultimately adopted for each light curve.

3.2. HERMES Spectroscopy

A new series of high-resolution echelle spectra were secured in 2011 December (36 exposures) and 2012 February (8 exposures) with HERMES, the fiber-fed high-resolution spectrograph on the Mercator telescope located at the Observatorio del Roque de los Muchachos, La Palma, Canary Islands. HERMES samples the entire optical wavelength range (3800–9000 Å) with a resolution of $R = 85,000$ (Raskin et al. 2011). The observations listed in Table 3 cover the orbital cycle uniformly. Groups of two concatenated exposures allow us to obtain a robust estimation of random noise as a function of wavelength and a check on cosmic-ray events surviving the detection algorithm in the data reduction. In total, 44 exposures were obtained at 19 epochs, 16 of which are out of eclipse. One series of six exposures starts near the primary mid-eclipse. One series of two concatenated exposures taken around secondary mid-eclipse has a significantly lower exposure level, but another one consisting of four concatenated exposures starting around secondary mid-eclipse is available.

Exposure times close to 2100 s were used for most spectra, but in case of one out-of-eclipse epoch, the exposure time was significantly shorter, 1200 s. The signal-to-noise ratio of the spectra is 50–100 at 4000 Å, rapidly increasing to 120 to 200 at 5000 Å, and remaining close to this level at longer wavelengths. The numbers apply to the sum of two concatenated exposures.

Table 3
HERMES Observations

Phase	BJD−2,450,000.000	Exp Time (s)
0.9957	5904.586	2100
0.0060	5904.611	2100
0.0168	5904.637	2100
0.0272	5904.662	2100
0.0376	5904.687	1980
0.0476	5904.711	1980
0.0613	5909.561	1500
0.0692	5909.580	1500
0.1128	5914.502	2100
0.1231	5914.527	2100
0.1530	5914.599	2100
0.1634	5914.624	2100
0.2259	5907.549	2100
0.2363	5907.574	2100
0.2803	5912.497	2100
0.2907	5912.522	2100
0.3434	5912.649	2100
0.3534	5912.673	2100
0.4432	5905.664	2100
0.4449	5910.485	2300
0.4536	5905.689	2100
0.4565	5910.513	2300
0.4673	5910.539	2100
0.4777	5910.564	2100
0.5010	5910.620	2100
0.5113	5910.645	2100
0.6427	5908.553	2200
0.6535	5908.579	2200
0.7187	5913.553	2100
0.7291	5913.578	2100
0.7945	5906.510	2100
0.8049	5906.535	2100
0.9278	5911.648	2200
0.9390	5911.675	2200

Notes. Time series HERMES spectroscopy of V578 Mon. Each exposure is less than 0.01 of the orbital period for V578 Mon of 2.4084822 days. The time series spectra were obtained to cover the out-of-eclipse, primary eclipse, and secondary eclipse phases.

The reduction of the spectra has been performed using the HERES pipeline software package. The spectra resampled directly in constant-size velocity bins (ln λ), which are very nearly the size of the detector pixels, were used. Normalization to the continuum is done separately.

The HERMES spectra outnumber the CASPEC spectra used by Hensberge et al. (2000), but fall short with regard to signal-to-noise ratio. However, they cover a much larger wavelength region, include epochs in both eclipses, and cover the orbit more homogeneously. In the wavelength region covered by both sets, the reconstruction has better signal-to-noise ratio in the CASPEC set, but the risk of bias due to phase gaps might be higher with the CASPEC data. Both data sets were obtained in different parts of the apsidal motion cycle.

4. ANALYSIS

4.1. Spectral Disentangling and Light Ratio

In the V578 Mon binary system, the eclipses are partial, which causes degeneracy in the light curve solution for the radii of the components. It was checked whether a spectroscopic light ratio has sufficient precision to reduce the degeneracy. This light ratio might be constrained either by the changing line dilution during

Table 4
Radial Velocity Solutions

	q	K_1 (km s^{-1})	K_2 (km s^{-1})	e
Hensberge et al. (2000) (LC+spectroscopy)	0.7078 ± 0.0002	259.8	183.9	0.0867
Hensberge et al. (2000) RV only	0.705 ± 0.004	259.8 ± 0.8	184.4	0.0836 ± 0.0008
HERMES spectra, e fixed	0.710	259.8	184.5	0.07755
HERMES spectra, e and ω fixed	0.709	259.4	184.0	0.07755

the eclipse, and/or by constrained fitting of the reconstructed component spectra by theoretical spectra, simultaneously deriving the light ratio as well as the photospheric parameters (Tamajo et al. 2011). In the latter implementation, the light ratio is assumed identical in all observed spectra, hence eclipse spectra are not used.

With partial eclipses of roughly 0.1 mag depth and less for the secondary eclipse at the epoch of the spectroscopy, the line depth in the composite spectrum is affected at the level of 0.5% of the continuum only when the two components have in their intrinsic spectra a line differing by 7% of the continuum depth. The similarity of the components and the rotational broadening in the spectra imply that no metal line approaches this level. Hence, using the changing line dilution to measure the light ratio precisely is challenging. Exceedingly large signal-to-noise ratios would be required to be able to use single or few lines. Including many lines, i.e., large stretches of spectrum offers the opportunity to reduce the requirements on the signal-to-noise ratio. However, bias in tracing the continuum is expected to put an upper limit on the precision with which the light ratio can be measured in a system with components with similar spectra and substantial rotation.

Therefore, we explored the alternative option of constrained fitting, although it is model-sensitive. Spectral disentangling (Hadrava 1995), further referred to as SPD is performed in a spectral range of about 100–150 Å (of the order of 4000 bins) in the wavelength range 3900–5000 Å, centered on prominent lines of He I, He II, and stronger metal lines. The apsidal motion study (Garcia et al. 2011) permitted us to fix the eccentricity e, the longitude of the periastron, ω, for the epoch of the spectra, and the time of periastron passage. The SPD code used is FDBINARY[9] (Ilijic et al. 2004).

SPD was applied to selected spectral regions of the HERMES spectra, well distributed over the full range of Doppler shifts in the orbit (see orbital phases in Table 3), leads to radial velocity amplitudes K1 and K2 compatible with Hensberge et al. (2000) within better than 1 km s^{-1}. Thus, the spectra are reconstructed using the mean orbital elements (Table 4), now also including regions around H$_\gamma$ and H$_\delta$ (H$_\beta$ has a broad interstellar band centered on its red wing). For the constrained fitting, optimization was done for hydrogen and helium lines only, and for combinations of them. The reconstructed spectra for both out-of-eclipse and in-eclipse phases are shown in Figures 2 and 3.

The component spectra for different dilution factors can be obtained from a single disentangling computation, followed by an adequate re-normalization. As a starting point for the photospheric parameters, $T_{\rm eff,1} = 30,000\,{\rm K}$ and $T_{\rm eff,2} = 26,400\,{\rm K}$ are used based on the extensive study of Hensberge et al. (2000) and Pavlovski & Hensberge (2005). The surface gravities of the components are fixed to $\log g_1 = 4.133 \pm 0.018$ and $\log g_2 =$
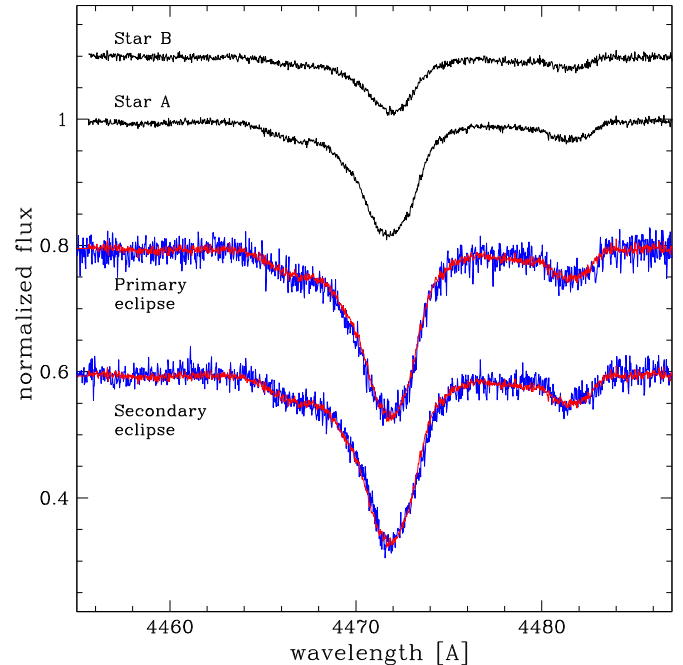
Figure 2. Fits (red) to the HERMES spectra (blue) obtained during the primary and secondary eclipse of V578 Mon. The disentangled component spectra obtained from time series of observed spectra out of eclipse are shown above in black. The light ratio from the light curve analysis agrees to within the uncertainty with the light ratio derived from the in-eclipse spectra. The light contribution of each component in the phases of the eclipses was calculated from the final light curve solution.

(A color version of this figure is available in the online journal.)

4.185 ± 0.021 as derived in this paper. This suppresses the degeneracy of line profiles of hot stars in the (temperature, gravity) plane. Calculations for a small grid in $\log g$ have shown that the effect of fixing $\log g$ might produce deviations of about a few tenths of the percentage in determining the light dilution factors.

Optimization of relative light factors includes a search through a grid of theoretical spectra, using a genetic algorithm. A grid of synthetic spectra was calculated assuming non-LTE line formation. The calculations are based on the so-called hybrid approach of Nieva & Przybilla (2007) in which model atmospheres are calculated in LTE approximation and non-LTE spectral synthesis with detailed statistical balance. Model atmospheres are constructed with ATLAS9 for solar metallicity, [M/H] = 0, and helium abundance by number density, $N_{\rm He}/N_{\rm tot} = 0.089$ (Castelli et al. 1997). Non-LTE level populations and model spectra were computed with recent versions of DETAIL and SURFACE (Butler & Giddings 1985). Further details on the method, grid, and calculations can be found in Tamajo et al. (2011) and Pavlovski et al. (2009).

Depending on the line(s) included, the primary is found to contribute 68%–72% of the total light, with hydrogen lines supporting the larger fractions. Hydrogen suggests a few percent
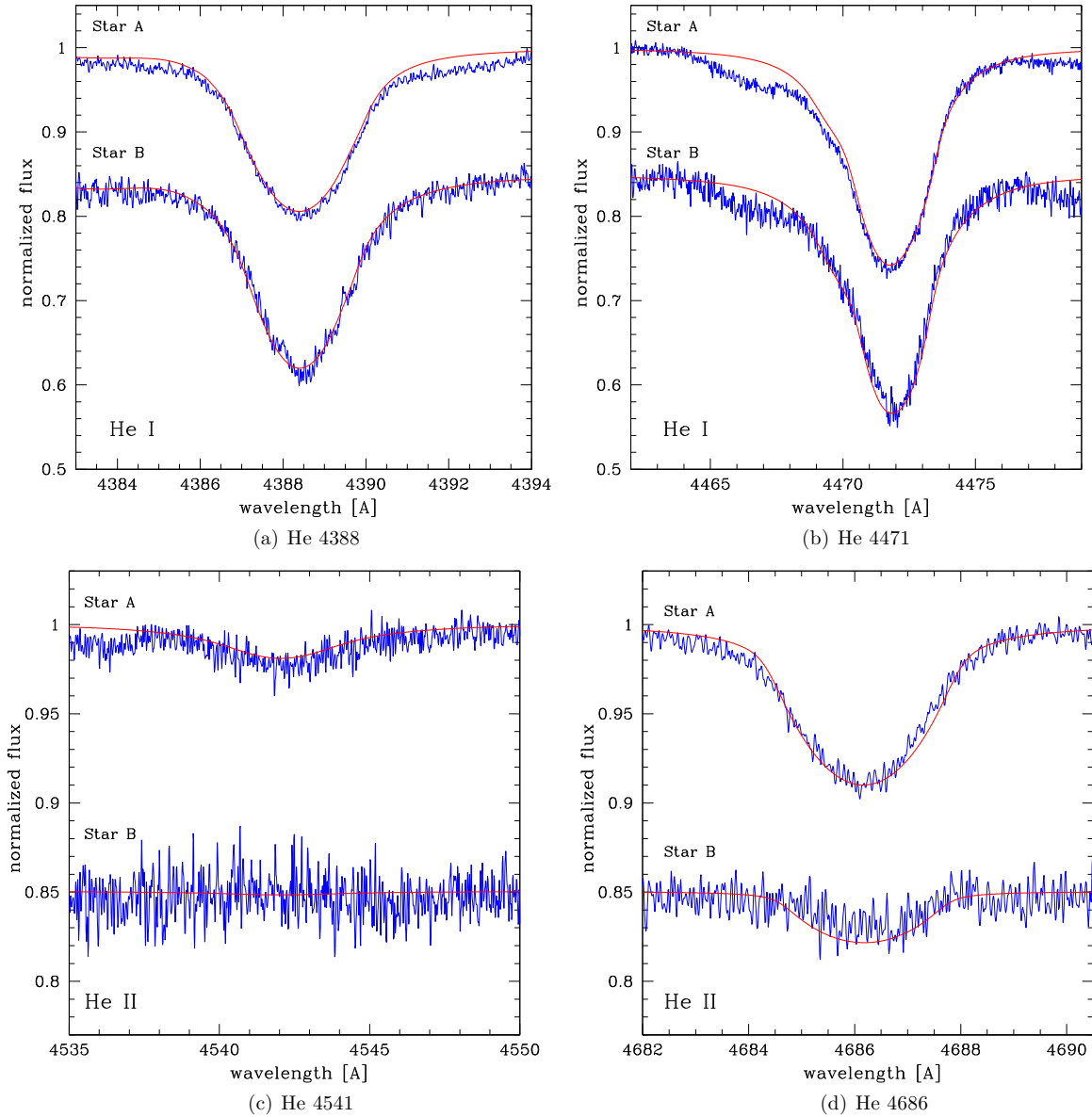
Figure 3. Optimal fitting for the four helium lines, He I 4388 Å, He I 4471 Å, He II 4541 Å, and He II 4686 Å, for the out-of-eclipse HERMES spectra. In each panel, helium line profiles for both components are shown (blue solid line). Optimal fitting was performed on all four lines simultaneously (red solid line). These are reconstructed helium profiles from disentangled spectra using the light ratio and surface gravities fixed to the final solution.
(A color version of this figure is available in the online journal.)

lower temperature for the primary, compared to the starting values. This is compatible with the tendency seen in Figure 7 of Hensberge et al. (2000), that H and He lines for the primary only marginally agree in effective temperature (taking the minimum χ^2 at the relevant gravity, a 1000 K difference in temperature estimation occurs).

The inconsistency between different indicators underlines the importance of developing a more consistent atmosphere model for these stars. One way, following Nieva & Przybilla (2012), is to include more ionization equilibria by analyzing the full wavelength range covered by the new spectra. This work-intensive analysis is out of the scope of the present paper, but probably indispensable to better constrain the degeneracy in the determination of the radii. Its success might be limited by the rotational broadening in the spectra. Another point of attention is the need to take into account temperature and gravity variations over the surface, due to the slightly non-spherical shape of the stars. Our work shows that the purely photometrically estimated light factors (Table 5) lie within the broader range of light factors (primary to total light) derived from the HERMES spectra, 0.68–0.72. However, one should be mindful that further improvement is needed—the spectroscopic estimates may be biased as different indicators are not yet fully compatible.

4.2. Light Curve Analysis

We use EB modeling software PHOEBE (Prša & Zwitter 2005) based on the Wilson–Devinney code (Wilson & Devinney 1971; Wilson 1979) for our light curve analysis. We fit light curves spanning 40 yr, covering one full apsidal motion cycle, in Johnson *UBV* and Strömgren *uvby* photometry.

Figures 4–7 are the residuals (data model) for our global best-fit model to the light curves for every light curve epoch

Table 5
Light Fraction Comparison

Method	Wavelength λ (nm)	Light Fraction ($l_1/l_1 + l_2$)
Light curve analysis (this work)	Johnson U, 365	0.706 ± 0.008
	Johnson B, 445	0.689 ± 0.007
	Johnson V, 551	0.683 ± 0.007
	Stromgren u, 365	0.710 ± 0.007
	Stromgren v, 411	0.690 ± 0.008
	Stromgren b, 467	0.685 ± 0.007
	Stromgren y, 547	0.683 ± 0.007
Hensberge et al. (2000)	Stromgren v, 411	0.675 ± 0.006
	Stromgren b, 467	0.683 ± 0.006
	Stromgren y, 547	0.692 ± 0.006
HERMES spectroscopy	400–500	0.700 ± 0.02

and filter in Table 2. Overall, the residuals are small—typically ≈ 0.005 mag. The residuals are significantly larger for light curve epochs 1970–1984 since error bars on the photometry data points measured using photometric plates are larger. We explore ranges for our light curve parameters as listed in Table 6. Our global best-fit matches observations well—the final light curve parameters Ω_1, Ω_2, i, and (T_2/T_1) are listed in Table 7.

4.2.1. Setup

For our global best-fit light curve model, we adopt a square root limb darkening (LD) law (Claret 2000), a B1V spectral type for the primary star implying $T_1 = 30,000$ K (Hensberge et al. 2000), no light reflection, and no third light.

We have four light curve parameters of interest—the primary potential Ω_1, the secondary potential Ω_2, the inclination i and the temperature ratio T_2/T_1. A parameter of interest is defined as a parameter that is varied to compute our confidence intervals. We determine these parameters and their uncertainties by mapping χ^2 space. The potential Ω is a modified Kopal potential for asynchronous, eccentric orbits (Wilson 1979). This potential ($\Omega \propto R^{-1}$) takes into account contributions from the star itself, its companion, the star's rotation about its axis, and the star's rotation in its orbit.

Our fixed parameters are the argument of periastron w_0, eccentricity e, apsidal motion $\dot{\omega}$, semi-major axis a, mass ratio q, period P, ephemeris HJD_0, systemic velocity γ, gravity brightening coefficients g_1 and g_2, primary and secondary synchronicity parameters F_1 and F_2, and albedos A_1 and A_2. We fix the argument of periastron w_0, eccentricity e, and apsidal motion $\dot{\omega}$ to values determined by a multi-epoch light curve analysis from Garcia et al. (2011). We fix the mass ratio $q \equiv (M_2/M_1)$, semi-major axis a, orbital period P, time of minima HJD_0, and systemic velocity γ to values from the Hensberge et al. (2000) analysis of the spectroscopic orbit. As mentioned previously, our HERMES spectral analysis derives radial velocity amplitudes K_1 and K_2 in agreement with the Hensberge et al. (2000) spectroscopic orbit (see Table 4). We adopt gravity brightening coefficients (g_1, g_2) and surface albedos (A_1, A_2) of 1.0 as appropriate for stars with radiative envelopes. The gravity brightening coefficient $g_1 = g_2 = 1.0$ for stars with radiative envelopes was first found by von Zeipel (1924). We fixed rotational synchronicity parameters $F_1 = 1.13$ and $F_2 = 1.11$ to values from Hensberge et al. (2000). Our limb darkening coefficients follow the square root law for hot stars (Claret 2000) and are listed in Table 8.
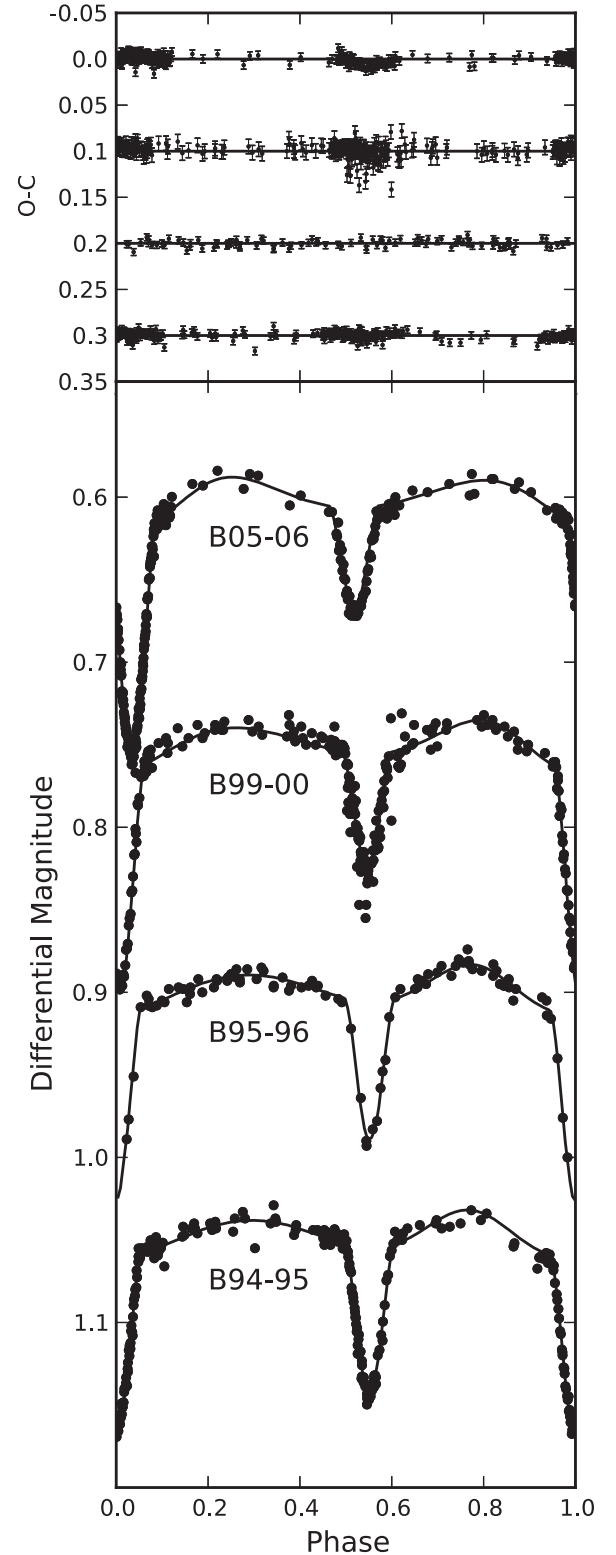

Figure 4. Representative fits to light curves from 2005–2006, 1999–2000, 1995–1996, and 1994–1995 in the Johnson B passband from global fits to all light curve data, offset for clarity. The residuals to the fits ($O - C$) are shown above.

(Supplemental data for this figure are available in the online journal.)

4.2.2. Fitting Method

Our fitting method is adapted from Y. Gómez Maqueo Chew et al. (2014, in preparation). We determine our best-fit

Table 6
Light Curve Parameter Ranges Explored

Parameter	Max	Min	Coarse Grid Spacing	Fine Grid Spacing
Primary surface potential, Ω_1	5.36	4.80	0.045	0.005
Secondary surface potential, Ω_2	5.26	4.40	0.045	0.005
Inclination, i (deg)	73.15	70.00	0.2	0.0005
Temperature ratio, (T_2/T_1)	0.875	0.843	0.0012	0.03

Table 7
Light Curve Analysis Results and Comparison

Light Curve Parameters	This Work & Garcia et al. (2011)	H2000
Primary surface potential, Ω_1	4.88 ± 0.03	5.02 ± 0.05
Secondary surface potential, Ω_2	4.89 ± 0.04	4.87 ± 0.06
Temperature ratio, (T_2/T_1)	0.858 ± 0.002	0.88 ± 0.02
Inclination, i (deg)	72.09 ± 0.06	72.58 ± 0.3
Eccentricity, e	$0.07755^{+0.00018}_{-0.00026}$	0.0867 ± 0.0006
Angle of periastron, w (deg)	159.8 ± 0.33	153.3 ± 0.6
Ephemeris, HJD_0 (days)	2449360.6250	2449360.6250
Total apsidal motion, $\dot{\omega}_{tot}$ (deg cycle^{-1})	$0.07089^{+0.00021}_{-0.00013}$	
Light curve filters	Strömgren $uvby$,	Strömgren $uvby$
Light curve filters	Johnson UBV	
Total light curve points	3489	992

Notes. The uncertainties on light curve parameters Ω_1, Ω_2, i, and T_2/T_1 are determined from confidence intervals in Figure 8. Light curve parameters e, w, and $\dot{\omega}_{tot}$ are taken from Garcia et al. (2011). This work utilizes photometry that span one full apsidal motion period ($U = 33.48^{+0.10}_{-0.06}$ yr). In contrast to the Hensberge et al. (2000) analysis, this work incorporates apsidal motion in the light curve model. Finally, the temperature ratio from Hensberge et al. (2000) is measured from spectral disentangling.

Table 8
Limb Darkening Coefficients

Filter	x_1	x_2	y_1	y_2
Square root law (adopted)				
Strömgren u	-0.096	-0.073	0.631	0.606
Strömgren b	-0.132	-0.115	0.672	0.659
Strömgren v	-0.129	-0.106	0.607	0.581
Strömgren y	-0.073	-0.044	0.612	0.581
Johnson U	-0.131	-0.115	0.685	0.675
Johnson B	-0.131	-0.110	0.654	0.638
Johnson V	-0.126	-0.105	0.602	0.578
Linear law				
Strömgren u	0.282	0.291	0.000	0.000
Strömgren b	0.272	0.281	0.000	0.000
Strömgren v	0.235	0.243	0.000	0.000
Strömgren y	0.293	0.304	0.000	0.000
Johnson U	0.280	0.291	0.000	0.000
Johnson B	0.262	0.273	0.000	0.000
Johnson V	0.235	0.242	0.000	0.000
Logarithmic law				
Strömgren u	0.450	0.452	0.252	0.242
Strömgren b	0.450	0.457	0.268	0.264
Strömgren v	0.397	0.398	0.242	0.233
Strömgren y	0.456	0.459	0.244	0.232
Johnson U	0.462	0.471	0.274	0.270
Johnson B	0.436	0.444	0.261	0.256
Johnson V	0.395	0.396	0.241	0.231

Notes. Our best-fit model uses the square root limb darkening law. Fits with the linear cosine or logarithmic limb darkening law had little effect on our final light curve solution.

global light curve solution by finding a unique set of light curve parameters Ω_1, Ω_2, T_2/T_1, and i, that correspond to the minimum chi square, χ^2_{min}, in a well mapped grid of parameter space. The chi square is a function of the light curve parameters, $\chi^2 = \chi^2(\Omega_1, \Omega_2, (T_2/T_1), i)$. We map parameter space by computing χ^2 for a grid of $>10^5$ unique sets of these light curve parameters. We use our map of parameter space to compute the uncertainties on our light curve parameters using confidence intervals. Plots of $\Delta\chi^2$ versus stellar radii R_1, R_2, temperature ratio T_2/T_1, and inclination i with confidence intervals are shown in Figure 8.

The step-by-step procedure is as follows.

1. We sample a coarse grid of 10^4 points defined by a range of potential Ω_1, potential Ω_2, inclination i, and temperature ratio T_2/T_1. The parameter ranges and spacings are given in Table 6.

For each grid point, we fit only for the "light levels" in PHOEBE which is equivalent to the total light contribution from each star in the photometric bandpass. We avoid using the WD2003 differential corrections (DC) fitting algorithm within PHOEBE to fit our light curve parameters. The DC algorithm can fall into local minima when fitting for many parameters. We compute the total chi square χ^2_k for each light curve fit as the sum of the chi square χ^2_p at each passband and epoch:

$$\chi^2_k\left(\Omega_{1k}, \Omega_{2k}, \frac{T_{2k}}{T_1}, i_k\right) = \sum_p^{15} \frac{\chi^2_p}{\sigma^2_p}, \qquad (1)$$

where index k corresponds to a unique point in parameter space $(\Omega_{1k}, \Omega_{2k}, T_{2k}/T_1, i_k)$. χ^2_k is the total chi square over all light curves at a unique point k. Index p corresponds to a unique light curve passband epoch as specified in Table 2. The chi square at the specific passband χ^2_p is computed as

$$\chi^2_p = \sum_i^N \frac{(f - f_m)^2}{\sigma^2_i}, \qquad (2)$$

where $N = N_d - N_p = 3485$ is the number of photometry data points N_d minus the number of parameters of interest N_p over all light curve epochs. Each data point has an error bar σ_i. Each light curve at a specific epoch and filter has a multiplicative factor σ_p which takes into account the systematic error. Multiplicative factor σ_p is used to normalize the χ^2 such that $\chi^2_{min} = N$ or reduced $\chi^2_{min,red} = 1.0$. f is the total flux of the binary at an HJD, and flux f_m is the corresponding model. From our coarse grid, we find the minimum total chi square $\chi^2 = \chi^2_{min}$ in parameter space.

2. We adjust the error bars of the individual photometry data points for all light curves to take into account any systematic error. For the minimum χ^2_{min} solution, the passband σ_p is
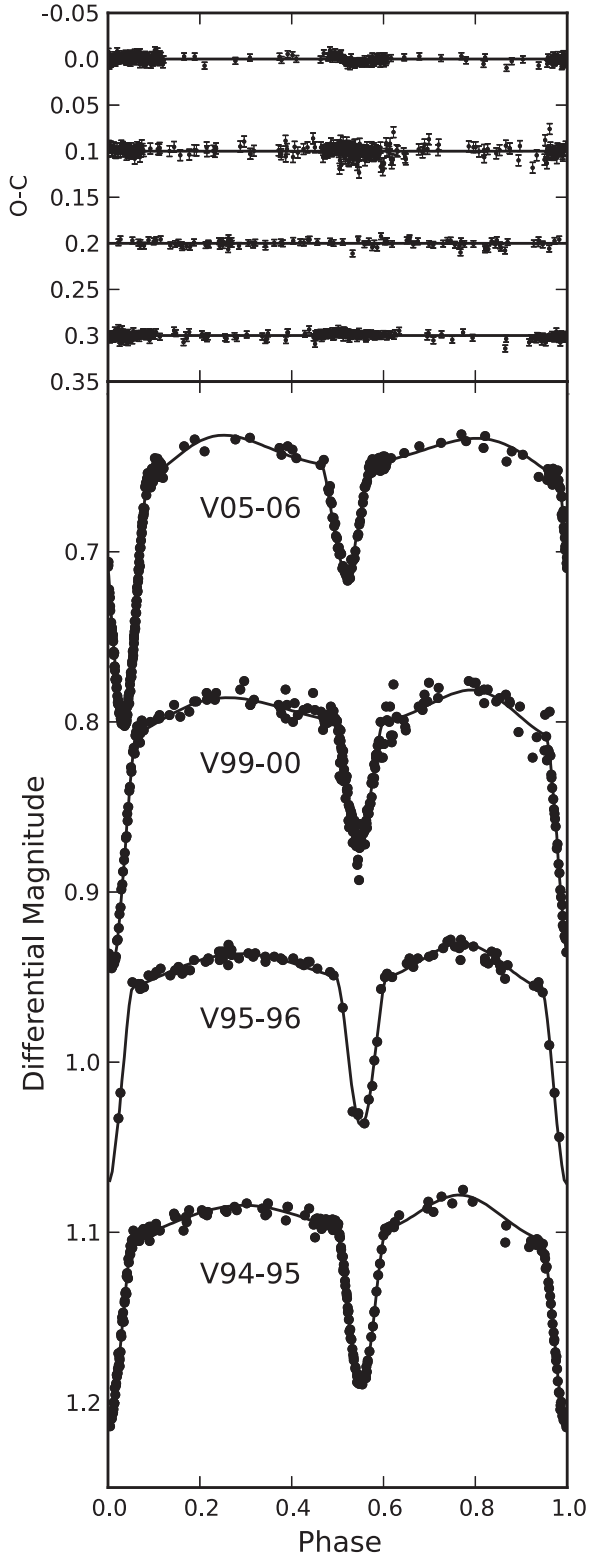
Figure 5. Same as Figure 4, but showing Johnson *V*-band light curves and fits.
(Supplemental data for this figure are available in the online journal.)
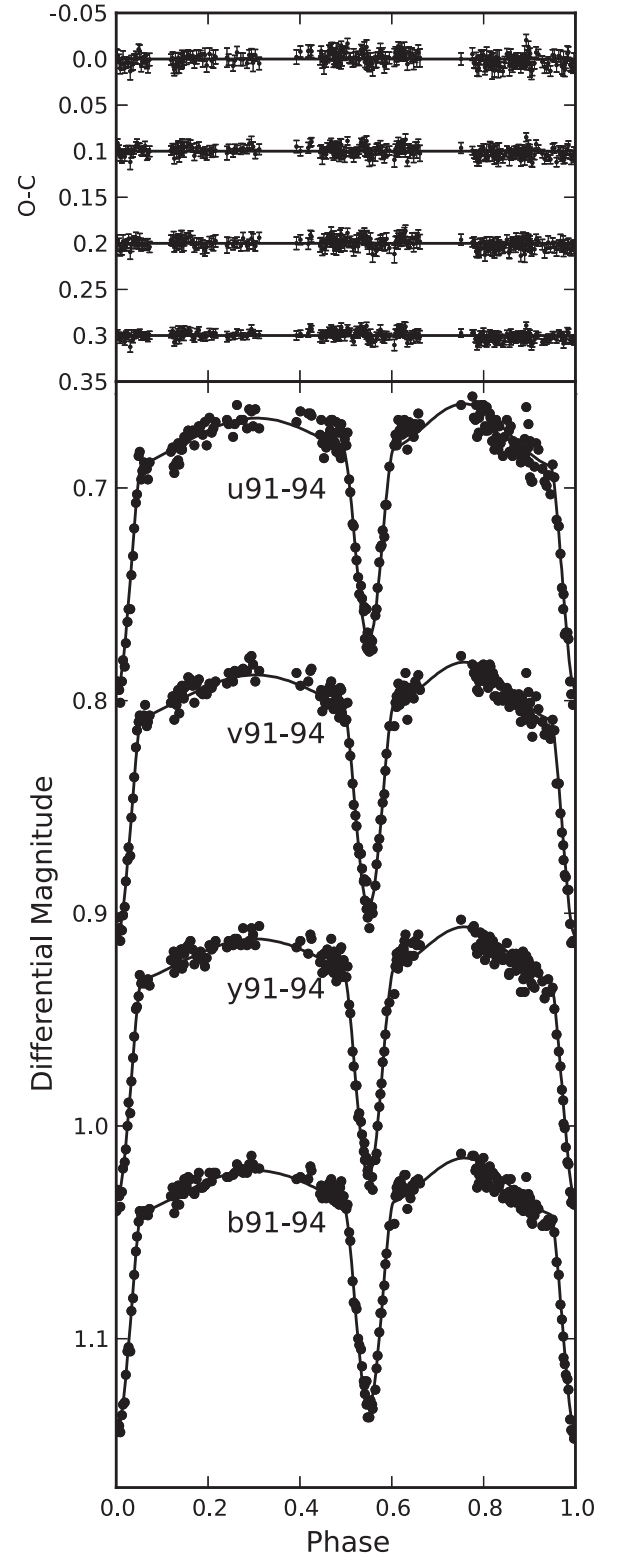

Figure 6. Same as Figure 4, but showing Strömgren *uvby* light curves and fits.
(Supplemental data for this figure are available in the online journal.)

computed for each separate light curve epoch and filter using the following equation:

$$\sigma_p = \sqrt{\frac{N}{\chi^2_{\min}}}, \qquad (3)$$

where $N = 3486$ as in step 1, and $\chi^2_{\min}$ is the minimum total χ^2 of the coarse grid. We choose to compute the multiplicative factor σ_p to weight each light curve such that the minimum reduced chi squared $\chi^2_{\min,\mathrm{red}} = 1.0$ for our global best-fit solution. We then rescale the χ^2 of all other light curve fits using the passband σ_p:
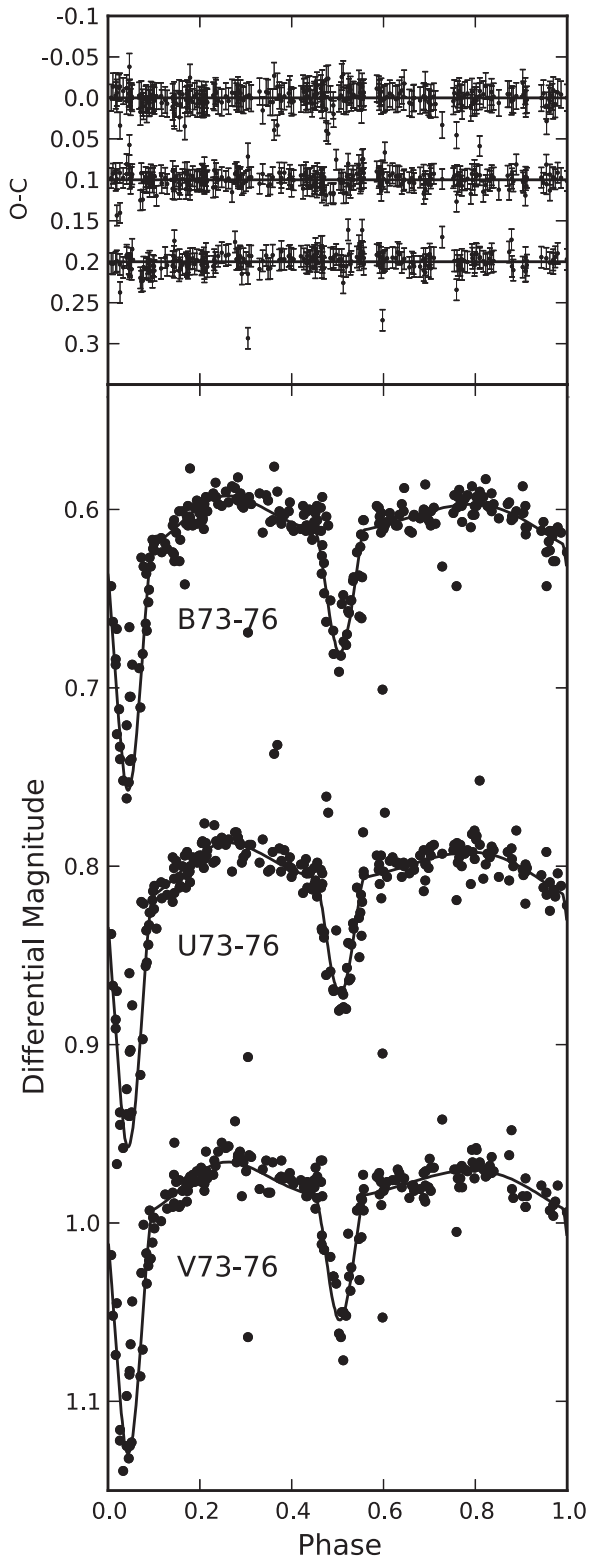
Figure 7. Same as Figure 4, but showing 1973–1977 Johnson *UBV* light curves and fits.

(Supplemental data for this figure are available in the online journal.)

$$\chi_k^2 = \sum_p^{15} \frac{\chi^2}{\sigma_p^2}, \tag{4}$$

where χ^2 is un-scaled and χ_k^2 is the scaled chi square at a unique point in parameter space k.

3. We perform steps 1 and 2 for a fine grid of $>10^5$ points in parameter space around the location of the minimum $\chi_{\min}^2$. In this way, we carefully map out parameter space at the location of the $\chi_{\min}^2$. We use multiple fine grids to precisely find our global best-fit minimum. The average grid spacings are 0.005, 0.005, 0.03, and 0.0005, respectively, for Ω_1, Ω_2, i, and T_2/T_1.

We find that the location of the minimum χ^2 moves slightly, and we recompute the multiplicative factor σ_p for each light curve to account for this, again making $\chi_{\min,red}^2 = 1.0$. Finally, we have a global best-fit solution within a finely sampled parameter space. Our global best-fit solution listed in Table 7 corresponds to the point in parameter space where chi square is scaled by σ_p such that $\chi_{\min,red}^2 = 1.0$.

4.2.3. A Comparison of Light Curve Models

In order to ensure that our light curve solution is robust and thus our light curve parameters are accurate, we compare our best-fit light curve model described above with several other models. As shown in Table 9, we find little effect on our best-fit light curve parameters from using different light curve models. All other models are not as favorable due to larger χ^2 or temperatures that do not agree with the analysis of the component spectra of V578 Mon from spectral disentangling of Hensberge et al. (2000).

For all the tests described below, we start at our best-fit solution, then fit all light curves in PHOEBE for primary potential Ω_1, secondary potential Ω_2, temperature ratio T_2/T_1, and inclination i. Our global best-fit uses a fixed primary temperature $T_1 = 30,000$ K, no light reflection, and no third light. Furthermore, our global best-fit uses fixed square root law limb darkening coefficients, which are found to work best for hot ($T_{eff} > 9000$ K) stars (Diaz-Cordoves & Gimenez 1992; van Hamme 1993). We discuss the different light curve models in the order in which they appear in our summary in Table 9.

1. *Fitting for Limb Darkening Coefficients.* We test the effect of fitting for square root law limb darkening coefficients, finding a lower chi square due to a larger number of free parameters. We find little effect on Ω_1, Ω_2, or i. However, we do find a much lower $T_2 = 25,049$. We reject this light curve model since $T_2 = 25,049$ is significantly outside of the acceptable range for $T_2 = 26,400 \pm 400$ from the spectral disentangling of Hensberge et al. (2000). We therefore perform another test: we keep T_2/T_1 fixed to our best-fit value, and fit for the limb darkening parameters, Ω_1, Ω_2, and i. We again find little effect on Ω_1, Ω_2, or i.

2. *Using a Different Limb Darkening Law.* We test the linear cosine and logarithmic limb darkening laws, finding little effect on our light curve parameters. The linear cosine law has a lower $\chi^2 = 3480.01$ than our best-fit model $\chi^2 = 3489.00$. The light curve model with logarithmic limb darkening has a larger $\chi^2 = 3503.96$-, and we therefore reject this model. See Table 8 for a list of the theoretical limb darkening coefficients for each light curve model that we test.

3. *Changing the Assumed Primary Star Temperature.* We test the effect of changing our adopted primary star effective temperature T_1. Our adopted primary temperature for our best-fit solution is $T_1 = 30,000 \pm 500$ K. Once again, we find little effect on Ω_1, Ω_2, i, or T_2/T_1.

We start with our best-fit global solution, but set $T_1 = 31,500$ K and $T_1 = 28,500$ K, 3σ above and below our adopted primary star effective temperature. Fits with lower
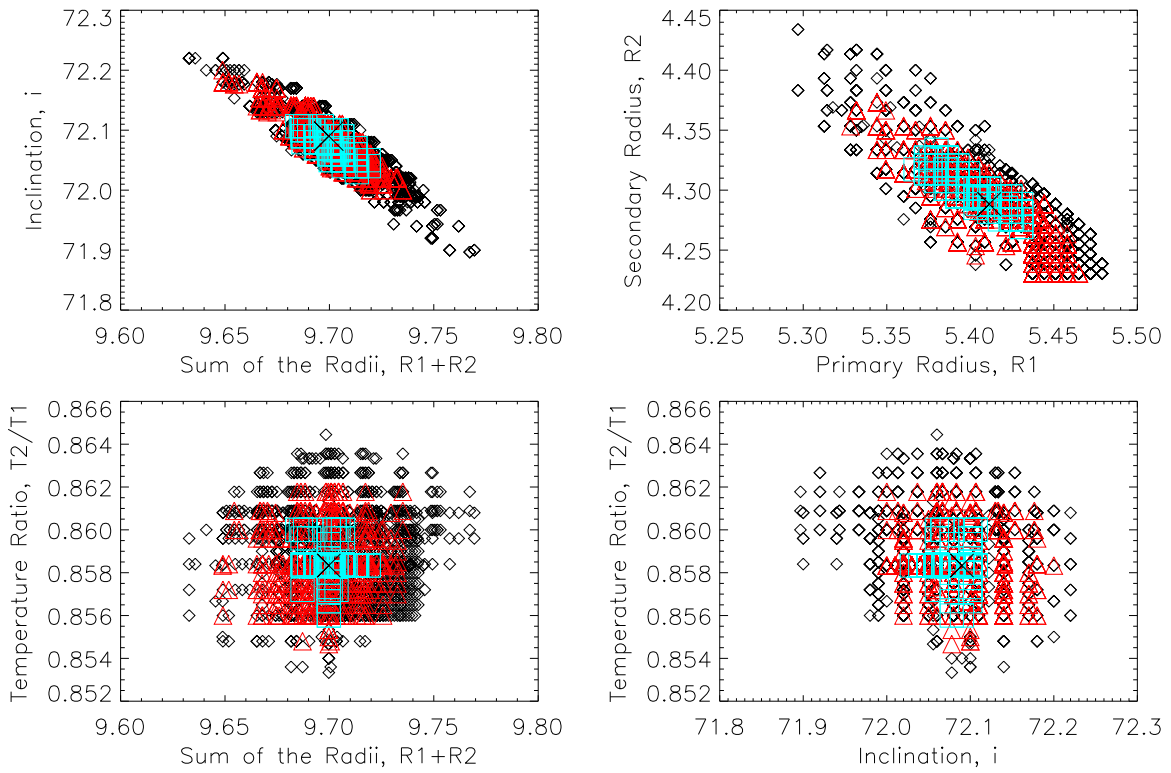
Figure 8. Degeneracies for our best-fit light curve solution. The blue squares, red triangles, and black diamonds correspond to differences in chi square from the global best-fit solution $\Delta\chi^2 = 4.72$, 9.70, and 16.3, respectively. For four parameters of interest, these $\Delta\chi^2$ correspond to 1σ, 2σ, and 3σ, respectively. There is a small degeneracy between the sum of the radii $R_1 + R_2$ and i. This degeneracy is typical for detached eclipsing binaries with circular or near circular orbits. Similarly, there is a small degeneracy between the primary and secondary radii R_1 and R_2. The global best-fit solution is marked with an X. There is no degeneracy between the temperature ratio T_2/T_1 and inclination i or sum of the radii $R_1 + R_2$.

(A color version of this figure is available in the online journal.)

Table 9
A Comparison of Light Curve Models

Model	Ω_1	Ω_2	i (deg)	(T_2/T_1)	χ^2
Best-fit	4.88 ± 0.03	4.89 ± 0.04	72.09 ± 0.06	0.858 ± 0.002	3489.00
Fitting for LD coefficients	4.92	4.89	72.18	0.835	3299.11
Linear law	4.92	4.89	72.15	0.860	3480.01
Logarithmic law	4.91	4.88	72.14	0.858	3503.96
Fix $T_1 = 28,500$	4.94	4.87	72.17	0.857	3460.16
Fix $T_1 = 31,500$	4.92	4.89	72.15	0.867	3488.01
Light reflection	4.90	4.92	72.20	0.856	3522.57
Third light	4.94	4.87	72.24	0.855	3414.93

Notes. The best-fit model uses the square root limb darkening law, a fixed $T_1 = 30,000$ K, no light reflection, and no third light.

primary temperature T_1 result in a better χ^2, however, $T_1 < 29{,}000$ K does not agree with the spectral disentangling analysis from Hensberge et al. (2000). This may be due to the fact that the PHOEBE light curve analysis constrains the temperature ratio and not the individual temperatures themselves. Further light curve tests at lower preferred temperatures T_1 and T_2 confirmed that changing effective temperatures has little effect on the geometric parameters, Ω_1, Ω_2, and i.

4. *Light Reflection.* We fit our light curve model with one light reflection. We find an inclination i larger by 2σ. However, the $\chi^2 = 3522.57$ is higher than our best-fit $\chi^2 = 3489.00$. We reject this model on this basis.

5. *Third Light.* We test the possibility of third light and its effect on our best-fit parameters. We fit for a third light

parameter starting from our best-fit light curve solution. The third light model has a lower χ^2 due to a larger number of free parameters. We find Ω_1 and i to be larger by 2σ and 2.5σ, respectively, from our best-fit model.

However, the third light parameter L_3 varies on the order of an apsidal period of the system. As shown in Table 10, we find at max a small contribution of third light $(L_3/L_{\rm tot}) \approx 0.045$ for the Johnson B filter of light curve epochs 1967–1984 and 2005–2006. This is likely due to PHOEBE using the L_3 parameter to minimize the small systematic error of 0.005 mag in the residuals of the 1967–1984 and 2005–2006 light curve epochs. Furthermore, the systemic velocity measured with the HERMES spectra and the CASPEC spectra in Hensberge et al. (2000) does not give any evidence for a large third body in the system that would

Table 10
Third Light

Observatory	Year	Filter	L_3/L_{tot}
APT	2005–2006	Johnson B	0.0441
		Johnson V	0.0218
APT	1999–2000	Johnson B	0.0158
		Johnson V	0.0080
APT	1995–1996	Johnson B	−0.0037
		Johnson V	0.0104
APT	1994–1995	Johnson B	0.0059
		Johnson V	0.0046
SAT	1991–1994	Strömgren u	−0.0116
		Strömgren v	−0.0004
		Strömgren b	0.0013
		Strömgren y	−0.0045
KPNO	1967–1984	Johnson U	0.0163
		Johnson B	0.0467
		Johnson V	−0.0100

Notes. Our best-fit light curve model includes no third light. The small amount of third light varies as a function of epoch.

contribute significantly to the light. This is consistent with the third light tests performed here.

4.2.4. Uncertainties on Light Curve Parameters

We compute uncertainties on each parameter of interest using confidence intervals as shown in Figure 8. From Press et al. (1988), for four parameters of interest, we find that 1σ, 2σ, and 3σ uncertainties correspond to solutions with confidence intervals of $\Delta\chi^2 = \chi^2 - \chi^2_{min,red} = 4.72$, 9.70, and 16.3, respectively. Here, χ^2_{min} is the minimum χ^2 of our global best-fit solution.

From Figure 8 we see small degeneracies between the geometric parameters, radii R_1, R_2, and inclination i. However, as expected, we do not see degeneracies between the geometric light curve parameters and the temperature ratio T_2/T_1.

Since T_2/T_1 is not strongly degenerate with these other parameters, we could potentially decrease the number of parameters of interest and in turn decrease the formal parameter uncertainties. Therefore, the uncertainties presented here are possibly conservative, given that we assume all degrees of freedom are parameters of interest (Avni 1976).

The small degeneracies in our parameters lead to uncertainties on potentials Ω_1 and Ω_2 of less than $<1.5\%$ error; this error already takes into account any systematic error in fitting the light curves, as detailed in Section 4.2.2. Similarly, the uncertainty on the temperature ratio (T_2/T_1) and inclination are also $<1\%$.

A source of systematic uncertainty unaccounted for from the confidence intervals and fitting procedure in Section 4.2.2 is from the comparison of light curve models detailed in Section 4.2.3 and Table 9. As shown in Table 9, all other light curve models assessed in Section 4.2.3, with the exception of using linear cosine LD parameters, are not as favorable as our best-fit model. The linear cosine model has a lower χ^2. Nevertheless, the inclination i, temperature ratio (T_2/T_1), and secondary potential Ω_2 are all within 1σ of our best-fit model. However, the primary potential for the linear cosine model $\Omega_1 = 4.92$ with our best-fit $\Omega_1 = 4.88 \pm 0.03$. Therefore our uncertainty on Ω_1 from our best-fit model could be slightly underestimated from these model comparisons.

4.2.5. Consistency of Light Fractions

As mentioned by Torres et al. (2010), an important consistency check of our light curve solution is that the light fractions $l_{f,1} = (l_1/l_1 + l_2)$ determined from spectroscopy and photometry agree. Given the small degeneracy between R_1 and R_2 as seen in Figure 8, we compare our photometrically determined light fraction with the light fraction from the HERMES spectral disentangling and a previous combined light curve and spectral disentangling analysis from Hensberge et al. (2000). We find that all three light fractions agree with each other to within 1.2σ. A comparison of light fractions is shown in Table 5.

For each of the $\approx 10^5$ light curve fits to our 40 yr of photometry data, we compute the light fraction at each of the passbands, Johnson UBV, and Strömgren $uvby$ photometry, $l_{f,1}(\lambda) = (l_1(\lambda)/l_1(\lambda) + l_2(\lambda))$, where $l_1(\lambda)$ and $l_2(\lambda)$ are the contribution of the primary and secondary star to the total light at a specific passband out of eclipse. The distribution of light fractions $l_{f,1}$ for light curve models with confidence intervals of 1σ and 2σ are shown in Figures 9 and 10.

4.3. Comparison with Hensberge et al. (2000)

Hensberge et al. (2000) uses an iterative, combined light curve and spectral disentangling analysis using the Wilson–Devinney light curve modeling program to compute their light curve parameters. We find that $R_1 = 5.23 \pm 0.06 \, R_\odot$ from Hensberge et al. (2000) is 2.5σ discrepant from our best-fit $R_1 = 5.41 \pm 0.04 \, R_\odot$. We find that our inclination $i = 72.09 \pm 0.06$ deg is 1.6σ discrepant from $i = 72.58 \pm 0.30$ deg from Hensberge et al. (2000). These discrepancies are likely due to the addition of apsidal motion and an updated eccentricity determined in Garcia et al. (2011). Apsidal motion and eccentricity can affect the potentials Ω_1 and Ω_2, and hence the determination of the radii at a low level. The potential Ω for a non-circular orbit is a function of eccentricity (see Wilson 1979). The addition of more light curve epochs may also play a role. Hensberge et al. (2000) only use the 1991–1994 light curve epoch with Strömgren $uvby$ photometry. As a check, we also recover the Hensberge et al. (2000) light curve solution when we fit only the 1991–1994 light curve epoch. Finally, simply the addition of more photometry data points may play a role. We use 3489 photometry data points in our light curve solution, whereas Hensberge et al. (2000) use 992. Our best-fit secondary radius $R_2 = 4.29 \pm 0.05 \, R_\odot$ is in agreement with $4.32 \pm 0.07 \, R_\odot$ from Hensberge et al. (2000). Our best-fit temperature ratio $(T_2/T_1) = 0.858 \pm 0.002$ is in agreement with the temperature ratio of 0.88 ± 0.020 from an analysis of the disentangled component spectra (Hensberge et al. 2000).

5. RESULTS: ABSOLUTE DIMENSIONS AND APSIDAL MOTION OF V578 MON

The absolute dimensions and other fundamental properties of V578 Mon are compiled in Table 11. Here we detail how each fundamental parameter for V578 Mon is computed in the order in which they appear in Table 11.

1. *Orbital Period.* We adopt an orbital period of $P = 2.4084822$ days from Hensberge et al. (2000).
2. *Masses.* The component masses $M_1 = 14.54 \pm 0.08 \, M_\odot$ and $M_2 = 10.29 \pm 0.06 \, M_\odot$ are determined from the spectroscopic orbit analysis from Hensberge et al. (2000). We do not use radial velocities from our HERMES spectroscopy
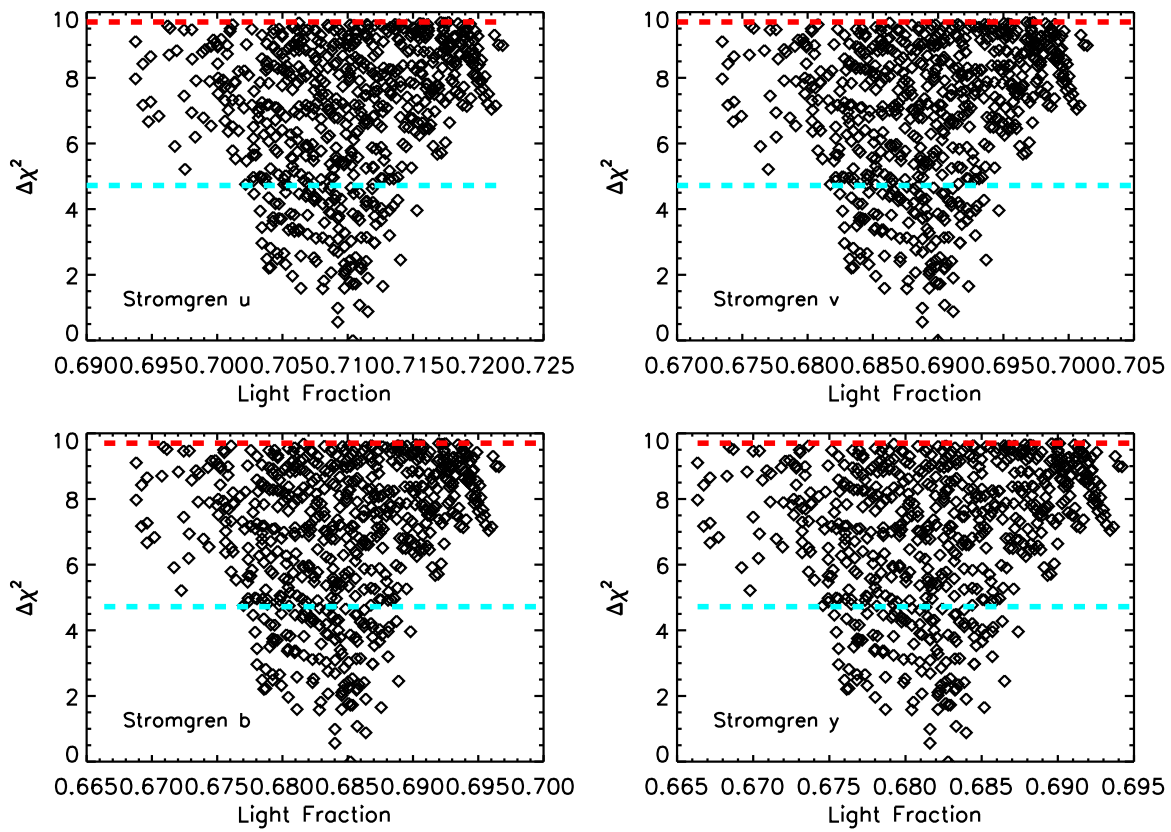
Figure 9. Light fractions $l_{f,1} = (l_1(\lambda)/l_1(\lambda) + l_2(\lambda))$ for light curve fits within 1σ (below the blue line) and 2σ (below the red line) uncertainty for the Stromgren *uvby* photometry. Our light fractions are consistent with the light fractions computed from Hensberge et al. (2000).

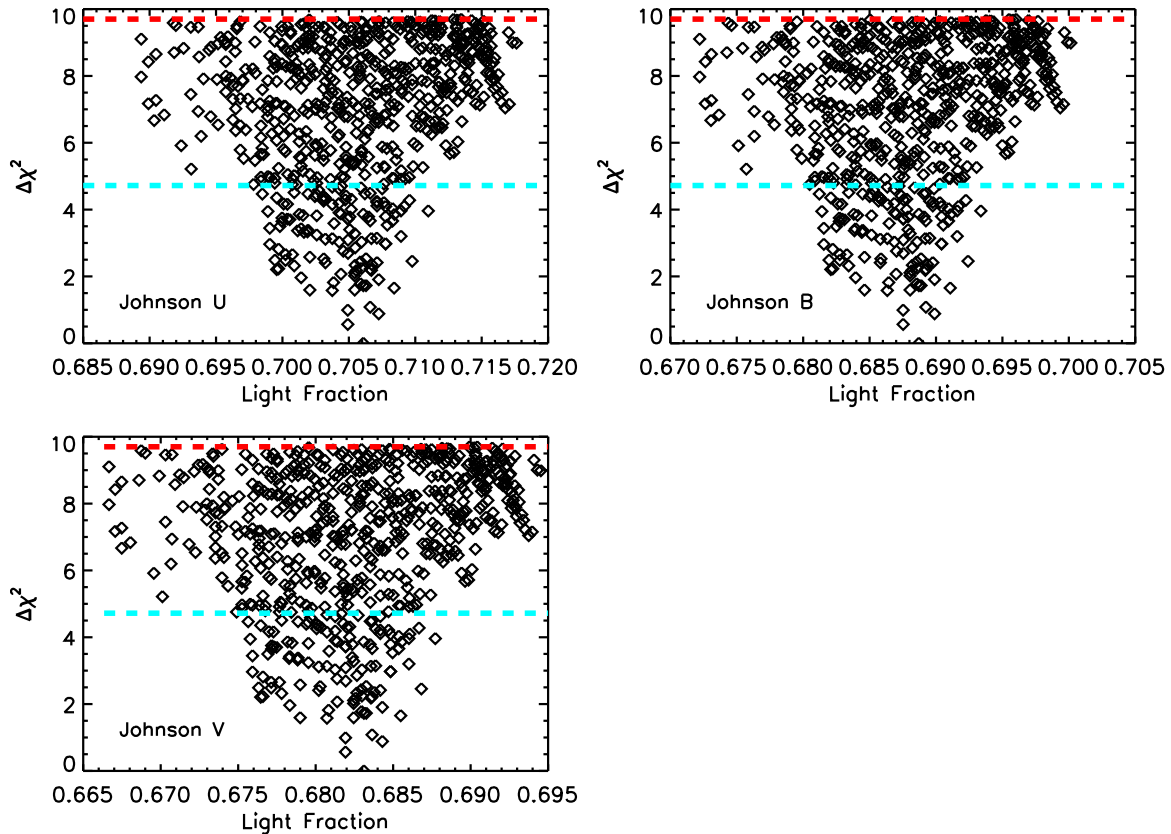(A color version of this figure is available in the online journal.)

Figure 10. Same as Figure 9 except for the Johnson *UBV* photometry.

(A color version of this figure is available in the online journal.)

Table 11
V578 Mon Absolute Dimensions

Parameter	Primary	Secondary
Orbital period, P (days)	2.4084822	
Mass, M ($M_\odot$)	14.54 ± 0.08	10.29 ± 0.06
Radius, R ($R_\odot$)	5.41 ± 0.04	4.29 ± 0.05
Effective temperature, $T_{\rm eff}$ (K)	$30{,}000 \pm 500$	$25{,}750 \pm 435$
Surface gravity, $\log g$ (cm s^{-2})	4.133 ± 0.018	4.185 ± 0.021
Surface velocity, $v_{\rm rot}$ (km s^{-1})	123 ± 5	99 ± 3
Luminosity, $\log \frac{L}{L_\odot}$	4.33 ± 0.03	3.86 ± 0.03
Synchronicity parameter, $F = \frac{w}{w_{\rm orb}}$	1.08 ± 0.04	1.10 ± 0.03
Apsidal period, U (yr)	$33.48^{+0.10}_{-0.06}$	
Observed Newtonian internal structure constant, $\log k_{2,\rm newt}$	-1.975 ± 0.017	

because the CASPEC spectra have higher signal-to-noise ratios, however, our analysis of the HERMES spectroscopy re-confirms the spectroscopic orbit.

3. *Radii.* We find precise uncertainties of $<1.5\%$ for the primary radius $R_1 = 5.41 \pm 0.04\,R_\odot$ and secondary radius $R_2 = 4.29 \pm 0.05\,R_\odot$ from our confidence intervals in Figure 8.

4. *Temperatures.* We find a 0.3% error on our temperature ratio $(T_2/T_1) = 0.858 \pm 0.002$ from our confidence intervals. Combined with the adopted temperature of the primary star, $T_1 = 30{,}000 \pm 500\,{\rm K}$ (Hensberge et al. 2000), our temperature ratio of T_2/T_1 yields a secondary temperature of $T_2 = 25{,}750 \pm 435\,{\rm K}$ via propagation of errors.

5. *Rotational Velocities.* We compute surface rotational velocities of $v_{1,\rm rot} = 123 \pm 5$ km s^{-1} and $v_{2,\rm rot} = 99 \pm 3$ km s^{-1} using the observed projected surface velocities $v_1 \sin i = 117 \pm 4$ km s^{-1} and $v_2 \sin i = 94 \pm 2$ km s^{-1} from Hensberge et al. (2000) and our inclination of $i = 72.09 \pm 0.06$. The uncertainty on rotational velocities is computed from propagating the error on the inclination i and the observed $v \sin i$.

6. *Surface Gravities.* We compute the surface gravity $\log g$ from our masses and radii, finding $\log g_1 = 4.133 \pm 0.018$ cm s^{-2} and $\log g_2 = 4.185 \pm 0.021$ cm s^{-2}. We compute the uncertainty on $\log g$ via error propagation:

$$\sigma_{\log g} = \sqrt{\left(\frac{\sigma_M}{M \ln 10}\right)^2 + \left(\frac{2\sigma_R}{R \ln 10}\right)^2}, \quad (5)$$

where σ_M is the uncertainty on the mass and σ_R is the uncertainty on the radius.

7. *Luminosities.* From our radii and temperatures, we compute luminosities for the primary and secondary star of $\log(L_1/L_\odot) = 4.33 \pm 0.03$ and $\log(L_2/L_\odot) = 3.86 \pm 0.03$. We compute the uncertainty on the luminosity using a similar error propagation as above, using errors from the temperature and radii, σ_T and σ_R.

8. *Synchronicity Parameters.* We find the components of V578 Mon to be close but not exactly tidally locked, with $F_1 = 1.08 \pm 0.04$ and $F_2 = 1.10 \pm 0.03$. The synchronicity parameter $F = w/w_{\rm orb}$, where w is the rotational velocity at the surface $v_{\rm rot}$ and $w_{\rm orb} = 2\pi R/P$ is the synchronous velocity. We compute the uncertainty via propagation of error from σ_R, error on inclination σ_i, and error on projected rotational velocities $\sigma_{v \sin i}$.

9. *Internal Structure Constant.* One of us (Dr. Claret) computed the Newtonian and general relativistic contributions

to the observed internal structure constant, $\log k_{2,\rm newt} = -1.975 \pm 0.017$ and $\log k_{2,\rm GR} = -3.412 \pm 0.018$.

6. THE STELLAR EVOLUTION MODELS AND TESTS

We compare the absolute dimensions of V578 Mon to the stellar evolution models of three separate groups: (1) Geneva models of Georgy et al. (2013) and Ekström et al. (2012), hereafter Geneva13; (2) Utrecht models of Brott et al. (2011), hereafter Utrecht11[10]; (3) Granada models of Claret (2004, 2006), hereafter Granada04. We assume that both stars have the same initial chemical composition and age, as expected for tight binary systems. We perform two tests: (1) the isochrone test, which tests the ability of stellar evolution models to produce stars with different masses, radii, temperatures, rotational velocities, and surface compositions at the same age, and (2) the apsidal motion test, which tests the ability of the stellar evolution models to reproduce the observed internal structure constant $\log k_2$ as determined from the observed apsidal motion.

A comparison of the basic input physics of the models is given in Table 12. The models use the same opacity tables of Iglesias & Rogers (1996). The mixing length $\alpha_{\rm MLT} \equiv l/H_p$ for all three sets of models differs by only 0.18 at maximum. The stellar evolution models use similar mass loss treatment from the prescription by Vink et al. (2001). Given the probable young age of V578 Mon due to its location in the open cluster NGC 2244 of the Rosette Nebula, the components of V578 Mon are not expected to have undergone significant mass loss (Vink et al. 2001).

However, all three sets of models differ on the choice of the convective core overshoot parameter $\alpha_{\rm ov}$. For the H and He burning phases of the convective core, the convective core size of the star is enlarged by $R_{\rm cc} = R_{cc}(1 + d_{\rm over}/H_p)$, where $\alpha_{\rm ov} \equiv d_{\rm over}/H_p$ in units of pressure scale height. The overshoot parameter is designed to account for the non-zero velocity of the material moving from the convective core to the radiative zone of the star. Observationally, a larger overshoot parameter means longer MS lifetimes for a given star, and thus older ages. The Geneva13 models use a small convective core overshoot of $\alpha_{\rm ov} = 0.1$ calibrated on the width of the MS for stars with masses $M = 1.35$–$9.0\,M_\odot$, which is characterized by the redmost point on the $B - V$, M_V H-R diagram (see Figure 8 of Ekström et al. 2012). The width of the MS is defined theoretically by the end of the hydrogen burning phase. The Utrecht11 models use a high convective core overshoot of $\alpha_{\rm ov} = 0.335$ which is calibrated using the observed width of the MS from the Very Large Telescope-FLAMES survey of B stars (Evans et al. 2005; Hunter et al. 2007). The convective core overshoot parameter $\alpha_{\rm ov} = 0.335$ is chosen such that a $16\,M_\odot$ star ends its MS lifetime when $\log g = 3.2$. This $\log g$ coincides with the drop in B star rotation rates in a $\log g$–$v \sin i$ diagram, which is interpreted as an estimate of the width of the MS for B stars. See Brott et al. (2011) for an in depth discussion. The Granada04 models utilize a moderate convective core overshoot $\alpha_{\rm ov} = 0.2$, though we performed several tests varying $\alpha_{\rm ov}$.

Rotationally driven mixing can bring more H and He from the envelope to the core, thus extending the MS lifetime of the star. Likewise, a larger overshoot parameter extends the size of the core, leading to a longer MS lifetime. The Granada04 models do not incorporate rotational mixing, while the Geneva13 and Utrecht11 models do. However, all three sets of models include rotation. All three sets of models use similar metallicity

---

[10] The Utrecht Stellar Evolution group is now located in Bonn, Germany.

Table 12
Stellar Evolution Model Comparison

Physical Input	Geneva13	Utrecht11	Granada04
Composition [Z,Y,X]	[0.014, 0.266, 0.720]	[0.0122, 0.2486, 0.7392]	[0.014, 0.271, 0.715]
Overshoot, α_{ov}	0.10	0.355	0.6 pri, 0.2 s
Mixing length, α_{MLT}	1.60	1.5	1.68
Rotation	Yes	Yes	Yes
Rotational mixing	Yes	Yes	No
Opacities	Iglesias & Rogers (1996)	Iglesias & Rogers (1996)	Iglesias & Rogers (1996)
Mass loss	Vink et al. (2001)	Vink et al. (2001)	Vink et al. (2001)

compositions of near solar. The initial bulk composition for V578 Mon is expected to be close to solar given that Mg surface abundance is within the error of the solar surface abundance despite the fact that several atmospheric abundances such as C, N, and O are somewhat metal poor compared with the Sun (Pavlovski & Hensberge 2005). This is because Mg abundance is not expected to be altered from the initial abundance in a star, where as C, N, and O atmospheric abundances could vary in V578 Mon due to rotational mixing (Lyubimkov et al. 2005). However, given that the C, N, and O atmospheric abundances of V578 Mon may be lower than solar, the metallicity of V578 Mon still remains as a source of systematic error in comparing the evolution models to the observations.

The Granada04 models also compute the internal structure constants $\log k_2$, $\log k_3$, and $\log k_4$ allowing for a test of the internal structure of V578 Mon via apsidal motion. Here we consider only the k_2 constant, given that k_3 and k_4 are very small. For V578 Mon, the tidal Love numbers quantify the deformation for each star's gravity field due to the companion.

6.1. Isochrone Test for V578 Mon

In Figure 11, we place the primary and secondary star on mass–radius and $\log g - \log T_{eff}$ isochrones for each set of models. For the stellar evolution models to pass the isochrone test, the models should predict a common age for both components of V578 Mon within the uncertainty. Given how different the masses of the primary and secondary stars of V578 Mon are, the isochrone test provides a stringent test of stellar evolution models. We also match all evolution models to the rotational velocities of the primary and secondary star.

We find several Geneva13, Utrecht11, and Granada04 models predict masses, radii, and temperatures for the components of V578 Mon that fall within the 1σ uncertainty of the measured absolute dimensions. Therefore, we estimate an age range for each star as shown in Table 12. The age difference for the Geneva13, Utrecht11, and Granada04 models is given as the smallest possible difference between the ages of the two stars given the age range of each star.

For the Geneva models, we use isochrones with initial rotational velocities of $(v_i/v_{crit}) = 0.30$ and $(v_i/v_{crit}) = 0.35$, which allow us to match the observed rotational velocities for each star. We interpolate the model evolution tracks for the primary and secondary star using the online interactive tool provided by the Geneva group.[11] Attempts to match the observed rotational velocities of V578 Mon with lower $((v_i/v_{crit}) < 0.30)$ or higher $((v_i/v_{crit}) > 0.40)$ initial velocities for either star were unsuccessful. Attempts to find a single initial rotational velocity to reproduce the current observed rotational velocities

for both stars with reasonable predicted radii and masses were also unsuccessful. However, given that V578 Mon is very near synchronization with the orbital period ($F_1 = 1.08 \pm 0.04$, $F_2 = 1.10 \pm 0.03$), the rotational history of V578 Mon could be different from the best matched v_i/v_{crit} found here. If the initial velocities of the components of V578 Mon were larger at the ZAMS than the orbital velocity, the stars could spin down to synchronize with the orbital velocity. Conversely, if v_i/v_{crit} was smaller than the orbital velocities, then the components of V578 Mon could spin up (Song et al. 2013). From Table 13, we find an age difference of 1.6 Myr for mass–radius isochrones and an age difference of only 0.1 Myr for $\log g - \log T_{eff}$ isochrones. It is easier to find consistency for the latter isochrones given our uncertainty in the effective temperatures of the two stars. We find that a primary radius of $R_1 = 5.50\ R_\odot$ and a secondary star radius of $R_2 = 5.20\ R_\odot$ yields common ages for the Geneva13 models. However, these radii are 3σ larger and 3σ smaller than our best-fit model, respectively.

For the Utrecht11 models, we use isochrones that match the observed surface velocities of the components of V578 Mon, $v_{1,rot} = 123 \pm 5\ \mathrm{km\,s^{-1}}$ and $v_{2,rot} = 99 \pm 3\ \mathrm{km\,s^{-1}}$. The Utrecht11 models are computed at very small steps of mass and initial rotational velocity, such that interpolating between model tracks is unnecessary. From Table 13, we see a marginally common age (age difference 0.4 Myr) for mass–radius isochrones, and a common age of 3.5 ± 1.5 Myr for $\log g - \log T_{eff}$ isochrones. The models were computed at solar metallicity by Dr. I. Brott (2014, private communication).

We compute the Granada04 models at the masses of the primary and secondary stars and chose rotational velocities to match the observed rotational velocities of V578 Mon. We attempt to match the absolute dimensions of V578 Mon to $\log g - \log T_{eff}$ or, alternatively, mass–radius isochrones for V578 Mon. We find an age gap of 1.5 Myr for mass–radius isochrones and a marginally common age for $\log g - \log T_{eff}$ isochrones when both stars have an overshoot of $\alpha_{ov} = 0.2$. Again, finding a match on the $\log g - \log T_{eff}$ isochrones is easier given the greater uncertainty in the effective temperatures.

In an attempt to match the ages of the two stars on a mass–radius isochrone, we also compute Granada04 models for $\alpha_{ov} = 0.4$ and $\alpha_{ov} = 0.6$. Figure 12 demonstrates the time evolution of the radii for V578 Mon for these different models. We find a near match on a single mass–radius isochrone with an age difference of only 0.2 Myr if we assume that the primary star has a convective overshoot of $\alpha_{ov} = 0.6$ and the secondary star has a convective overshoot of $\alpha_{ov} = 0.2$. We also find a common age of 5.5 ± 1.0 Myr for the $\log g - \log T_{eff}$ isochrone. This does not mean that an $\alpha_{ov} = 0.6$ for the primary star is correct for V578 Mon, merely that a higher convective overshoot allows
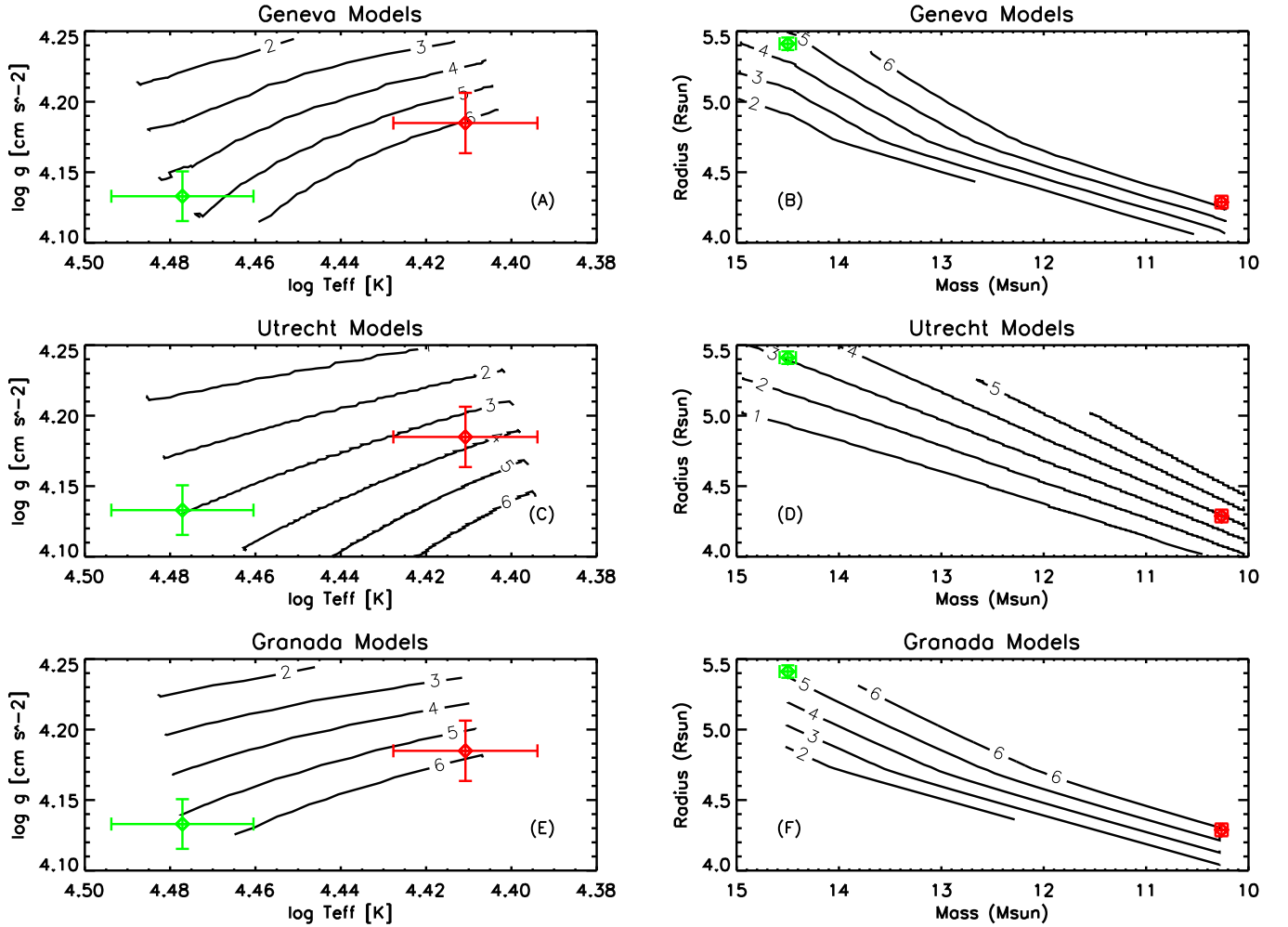

Figure 11. Best matches to observations: the Utrecht11 and Granada04 models. Both models use a larger than conventional overshoot of $\alpha_{ov} = 0.2$; see Table 13 for details. Isochrones are in steps of 1 Myr for the Geneva13, Utrecht11, and Granada04 models. The green point is the primary star, and the red point is the secondary star. All models have rotational velocities that match the observed velocities of V578 Mon $v_{1,rot} = 123 \pm 5$ km s^{-1} and $v_{2,rot} = 99 \pm 3$ km s^{-1}.

(A color version of this figure is available in the online journal.)

Table 13
Ages from Stellar Evolution Models

Model	Primary Age (Myr)	Secondary Age (Myr)	Age Diff (lower limit) (Myr)	α_{ov} (Scale Height)
	Mass$-$radius$-v_{rot}$ isochrones			
Geneva13	4.3–4.6	6.2–7.1	1.6	0.1
Utrecht11	3.0–3.2	3.6–4.4	0.4	0.355
Granada04	5.0–5.3	5.5–6.3	0.2	0.6 pri, 0.2 s
	log g–log T_{eff}–v_{rot} isochrones			
Geneva13	3.9–5.1	5.2–7.5	0.1	0.1
Utrecht11	2.6–3.8	2.4–5.2	Common age 3.5 ± 1.5	0.355
Granada04	4.7–5.5	4.9–6.8	Common age 5.5 ± 1.0	0.6 pri, 0.2 s

Notes. The ages for the primary and secondary stars are computed from evolutionary tracks at the masses of either star and solar metallicity. The Granada04 models were computed for a high convective overshoot of $\alpha_{ov} = 0.6$ pressure scale heights for the primary star, which allowed the models to match the observations. It is easier to find a common age for the log g − log T_{eff} isochrone given the larger uncertainty on the effective temperatures of the stars.

for compatible ages between the two stars. High convective overshoot has been found to work in matching other EBs on a single isochrone (Claret 2007).

In general, we find younger ages by ≈1 Myr for the Utrecht11 models of V578 Mon and similar ages for the Geneva13

and Granada04 models. This can be attributed to the larger convective overshoot of $\alpha_{ov} = 0.355$ included in Utrecht11 models compared with Geneva13 models ($\alpha_{ov} = 0.2$). While the primary star for the Granada04 models does have an even higher convective overshoot of $\alpha_{ov} = 0.6$, the models do not
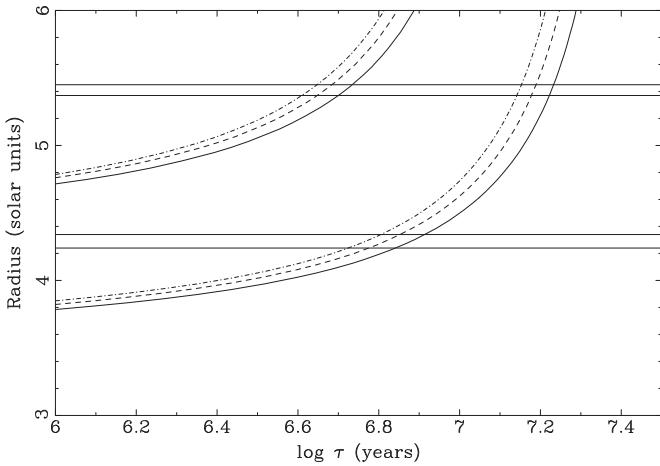
Figure 12. Time evolution of the radii for V578 Mon from Granada04 models computed for the masses of the V578 Mon primary and secondary. Dot-dashed, dashed, and solid lines are evolutionary models at a convective overshoot of α_{ov} of 0.2, 0.4, and 0.6 pressure scale heights, respectively. Horizontal lines are the upper and lower limits of the uncertainty on the primary star and secondary star radii, respectively. The models predict a common age of 5.5 Myr if we use a high convective overshoot of $\alpha_{ov} = 0.6$ evolution model for the primary star and $\alpha_{ov} = 0.2$ for the secondary star.

include rotational mixing, which also extends the MS lifetime of the stars.

6.2. Apsidal Motion Test for V578 Mon

Measurement of apsidal motion in eccentric binary systems allows for a stringent test of the internal structure constant $k_{2,\text{theo}}$ predicted from stellar evolution models (e.g., Claret & Giménez 2010). It is not possible to separate out each individual star's contribution to the apsidal period U from Newtonian apsidal motion.

The apsidal motion for V578 Mon was measured by Garcia et al. (2011). The observed apsidal motion of V578 Mon, $\dot{\omega}_{\text{tot}} = 0.07089^{+0.00021}_{-0.00013}$ deg cycle^{-1}, has contributions from both Newtonian and general relativity components (Claret & Giménez 2010):

$$\dot{\omega}_{\text{obs}} = \dot{\omega}_{\text{newt}} + \dot{\omega}_{\text{GR}}, \tag{6}$$

where $\dot{\omega}_{\text{GR}}$ is given by

$$\dot{\omega}_{\text{GR}} = 0.002286 \frac{M_1 + M_2}{a(1 - e^2)}. \tag{7}$$

We find that $\dot{\omega}_{\text{GR}} = 0.002589 \pm 0.000015$ which is only 4% of the Newtonian apsidal motion $\dot{\omega}_{\text{newt}} = 0.06830 \pm 0.00017$.

Both the Newtonian and general relativistic observed apsidal motions $\dot{\omega}_{\text{newt}}$ and $\dot{\omega}_{\text{GR}}$ have associated observed internal structure constants $k_{2,\text{obs}}$. The internal structure constant is twice the tidal Love number (Kramm et al. 2011), and is related to the density profiles, degree of sphericity, orbital parameters, masses, and rotation rates of both components of a binary star. Specifically, the internal structure constant is related to the solution of the Radau differential equation as in Equation (3) of Claret & Giménez (2010). Importantly, constant $k_{2,\text{obs}}$ is one the few ways to directly constrain the internal structure of stars.

From the precise observed apsidal motion, we compute the observed internal structure constant, $k_{2,\text{obs}} = k_{2,\text{obs}}(M_1, M_2, R_1, R_2, P, U, F_1, F_2, e)$, where U is the apsidal period, given by the equations (adopted from

Claret & Giménez 2010)

$$k_{2,\text{obs}} = \frac{1}{c_{21} + c_{22}} \frac{P}{U} \tag{8}$$

$$c_{2i} = \left[(F_i)^2 \left(1 + \frac{M_{3-i}}{M_i} \right) f(e) + 15 \frac{M_{3-i}}{M_i} g(e) \right] \left(\frac{R_i}{a} \right)^5 \tag{9}$$

$$f(e) = (1 - e^2)^{-2} \tag{10}$$

$$g(e) = \frac{(8 + 12e^2 + e^4) f(e)^{2.5}}{8}. \tag{11}$$

We compute the internal structure constant due to the Newtonian apsidal motion, $\log k_{2,\text{newt}} = -1.975 \pm 0.017$, and due to general relativity, $\log k_{2,\text{GR}} = -3.412 \pm 0.018$. The Newtonian apsidal motion is much larger than the general relativistic component, and therefore the internal structure constant is also much larger.

We compute the theoretical internal structure constant, $k_{2,\text{theo}}$ using the methods of Claret & Giménez (2010). The theoretical k_2 constant was corrected for by rotation (Claret 1999) and dynamical tides (Willems & Claret 2002). The theoretical internal structure constant is a combination of the internal structure constants for both stars, such that

$$k_{2,\text{theo}} = \frac{c_{21}k_{21} + c_{22}k_{22}}{c_{21} + c_{22}} \tag{12}$$

which can then be compared to observations.

We find the predicted Newtonian apsidal motion to be $\dot{\omega}_{\text{theo}} = 0.06883 \pm 0.00017$ and consequently the predicted Newtonian internal structure constant to be $\log k_{2,\text{theo}} = -2.005 \pm 0.025$. This is in very good agreement with the observed $\log k_{2,\text{obs}} = -1.975 \pm 0.017$. From Equation (9), the parameter c_{12} is about 67% larger than c_{22}. Therefore, the weighted contribution of the primary dominates the theoretical apsidal motion. V578 Mon is a relatively young system; therefore, $\log k_{2,\text{theo}}$ is almost constant during the early phases of stellar evolution. The apsidal motion test is therefore complementary to the isochrone test. Claret & Giménez (2010) compile a list of eclipsing binaries with apsidal motion, demonstrating good agreement between observed and predicted apsidal motions. V578 Mon continues this trend of agreement between theoretical and observational internal structure constants. For this relatively young system, matching the radii, temperatures, and masses of isochrones is key given that we have so few young massive EBs with non-equal mass ratios.

7. CONCLUSION

We have determined the absolute dimensions of the massive, detached eclipsing binary V578 Mon, which is a member of the young star-forming region NGC 2244 in the Rosette Nebula. We confirm that the previously published spectroscopic orbit of Hensberge et al. (2000) agrees with our current spectroscopic orbit of V578 Mon. From our HERMES spectra, we find that our photometric light ratio from the light curve analysis is fully compatible with the disentangled component spectra of V578 Mon.

From 40 yr of Johnson *UBV* and Strömgren *uvby* photometry we determine updated radii and measure the temperature ratio and light ratio for the components of V578 Mon. We determine

the radii to better than 1.5% accuracy and carefully map out parameter space in order to reveal any possible degeneracies. We also compare our global best-fit light curve model with models that include different limb darkening parameters, a different assumed temperature for the primary star, and light reflection or third light, finding little effect on our global model. We do not unambiguously rule out light reflection or a third body, but we confirm that these additional complications to the light curve model will not affect our final solution.

We have compared our observed masses, radii, temperatures, and rotational velocities to stellar evolution models of the Geneva, Utrecht, and Granada groups. We find no common match in predicted ages for mass–radius isochrones of the Geneva13 models. We find an age difference of only 0.1 Myr in predicted ages for the Geneva13 models for $\log g - \log T_{\rm eff}$ isochrones. For the Utrecht11 models, we find a marginally common predicted age with an age difference of only 0.4 Myr for the mass–radius isochrones. For the $\log g - \log T_{\rm eff}$ isochrones, we find common ages of 3.5 ± 1.5 Myr for the Utrecht11 models. For the Granada04 models, we find a small age gap of only 0.2 for the mass–radius isochrone when the primary star has a quite large convective overshoot of $\alpha_{\rm ov} = 0.6$. We do not find common ages for the mass–radius isochrone for the Granada04 models when the convective overshoot for both stars is a more moderate $\alpha_{\rm ov} = 0.2$.

This work suggests that models with larger convective overshoot predict a closer common age for the components of V578 Mon than models with a more conventional overshoot of $\alpha_{\rm ov} = 0.2$ pressure scale heights. Evolutionary models with larger convective overshoot extend the size of the convective core for massive stars, thus extending the MS lifetime and allowing for isochrones to predict a common age for V578 Mon. However, rotational mixing can also prolong the MS lifetime, making the two effects some what degenerate. The radii may in be slightly dependent upon effective temperatures, which are based on imperfect atmosphere models. Furthermore, there are small systematic residuals of 0.005 mag in the light curve fits which may slightly affect the radii. Finally, effects of binarity, while likely small, are not taken into account: the side of each star facing the other may be heated and the addition to the potential Ω from the companion is not taken into account in the models. The binarity of V578 Mon may cause single star models explored here to not be applicable.

Given the short apsidal period of V578 Mon of $33.48^{+0.10}_{-0.06}$ yr, our photometry covers one full apsidal motion period. Combined with our precise measurement of the radii of V578 Mon we compute the internal structure constant $\log k_2$ finding that our observed $\log k_{2,\rm obs} = -1.975 \pm 0.017$ in agreement with the theoretical internal structure constant $\log k_{2,\rm theo} = -2.005 \pm 0.025$.

V578 Mon is a particularly important system for testing stellar evolution models its given young age and the difference of $\approx30\%$ in the masses of the primary and secondary component star. B-type detached eclipsing binaries such as V1388 Ori and V1034 Sco have similar differences in mass of 40% and 50%, respectively, meaning these systems are also of particular importance to providing constraints on stellar evolution models. However, V578 Mon is unique among such systems by virtue of its young age, thus providing the strongest constraints on the models at the earliest stages of massive stellar evolution.

Future work may include comparing the carefully vetted sample of high mass EBs in the Torres et al. (2010) sample to evolutionary models, or may include more recent

massive EBs such as V 380 Cyg (Tkachenko et al. 2014), LMC 172231, and ST2-28 (Massey et al. 2012), to see if larger convective overshoot parameters allow for common predictions of age.

REFERENCES

Argelander, F. W. A. 1903, Bonner Durchmusterung des nordlichen Himmels (Bonn: Eds Marcus and Weber's Verlag), 0
Avni, Y. 1976, ApJ, 210, 642
Bell, S. A., Hilditch, R. W., & Adamson, A. J. 1986, MNRAS, 223, 513
Bouzid, M. Y., Sterken, C., & Pribulla, T. 2005, A&A, 437, 769
Brott, I., de Mink, S. E., Cantiello, M., et al. 2011, A&A, 530, A115
Butler, K., & Giddings, J. R. 1985, Newsletter of Analysis of Astronomical Spectra, No. 9 (London: Univ. of London), 723
Cannon, A. J., & Pickering, E. C. 1923, AnHar, 98, 1
Castelli, F., Gratton, R. G., & Kurucz, R. L. 1997, A&A, 318, 841
Claret, A. 1999, A&A, 350, 56
Claret, A. 2000, A&A, 363, 1081
Claret, A. 2004, A&A, 424, 919
Claret, A. 2006, A&A, 453, 769
Claret, A. 2007, A&A, 475, 1019
Claret, A., & Giménez, A. 2010, A&A, 519, A57
Diaz-Cordoves, J., & Gimenez, A. 1992, A&A, 259, 227
Ekström, S., Georgy, C., Eggenberger, P., et al. 2012, A&A, 537, A146
Evans, C. J., Smartt, S. J., Lee, J.-K., et al. 2005, A&A, 437, 467
Garcia, E. V., Stassun, K. G., Hebb, L., Gómez Maqueo Chew, Y., & Heiser, A. 2011, AJ, 142, 27
Garcia, E. V., Stassun, K. G., & Torres, G. 2013, ApJ, 769, 114
Georgy, C., Ekström, S., Granada, A., et al. 2013, A&A, 553, A24
Hadrava, P. 1995, A&AS, 114, 393
Heiser, A. M. 1977, AJ, 82, 973
Heiser, A. M. 2010, JAVSO, 38, 93
Hensberge, H., Pavlovski, K., & Verschueren, W. 2000, A&A, 358, 553
Hog, E., Kuzmin, A., Bastian, U., et al. 1998, A&A, 335, L65
Holmgren, D. E., Hill, G., & Fisher, W. 1990, A&A, 236, 409
Hunter, I., Dufton, P. L., Smartt, S. J., et al. 2007, A&A, 466, 277
Iglesias, C. A., & Rogers, F. J. 1996, ApJ, 464, 943
Ilijic, S., Hensberge, H., Pavlovski, K., & Freyhammer, L. M. 2004, in ASP Conf. Ser. 318, Spectroscopically and Spatially Resolving the Components of the Close Binary Stars, ed. R. W. Hilditch, H. Hensberge, & K. Pavlovski (San Francisco, CA: ASP), 111
Kramm, U., Nettelmann, N., Redmer, R., & Stevenson, D. J. 2011, A&A, 528, A18
Lyubimkov, L. S., Rostopchin, S. I., Rachkovskaya, T. M., Poklad, D. B., & Lambert, D. L. 2005, MNRAS, 358, 193
Massey, P., Morrell, N. I., Neugent, K. F., et al. 2012, ApJ, 748, 96
Nieva, M. F., & Przybilla, N. 2007, A&A, 467, 295
Nieva, M.-F., & Przybilla, N. 2012, A&A, 539, A143
Ogura, K., & Ishida, K. 1981, PASJ, 33, 149
Pavlovski, K., & Hensberge, H. 2005, A&A, 439, 309
Pavlovski, K., Tamajo, E., Koubský, P., et al. 2009, MNRAS, 400, 791
Popper, D. M. 1974, ApJ, 188, 559
Popper, D. M., & Etzel, P. B. 1981, AJ, 86, 102
Popper, D. M., & Hill, G. 1991, AJ, 101, 600
Press, W. H., Teukolsky, S. A., Vetterling, W. T., & Flannery, B. P. 1988, Numerical Recipes in C (2nd ed.; New York: Cambridge Univ. Press), 697

Pribulla, T., Rucinski, S. M., Latham, D. W., et al. 2010, AN, 331, 397
Prša, A., & Zwitter, T. 2005, ApJ, 628, 426
Raskin, G., van Winckel, H., Hensberge, H., et al. 2011, A&A, 526, A69
Song, H. F., Maeder, A., Meynet, G., et al. 2013, A&A, 556, A100
Southworth, J., Maxted, P. F. L., & Smalley, B. 2004, MNRAS, 351, 1277
Stickland, D. J., Koch, R. H., & Pfeiffer, R. J. 1992, Obs, 112, 277
Tamajo, E., Pavlovski, K., & Southworth, J. 2011, A&A, 526, A76
Tkachenko, A., Degroote, P., Aerts, C., et al. 2014, MNRAS, 438, 3093

Torres, G., Andersen, J., & Giménez, A. 2010, A&ARv, 18, 67
van Hamme, W. 1993, AJ, 106, 2096
Vink, J. S., de Koter, A., & Lamers, H. J. G. L. M. 2001, A&A, 369, 574
von Zeipel, H. 1924, MNRAS, 84, 665
Wang, J., Townsley, L. K., Feigelson, E. D., et al. 2008, ApJ, 675, 464
Willems, B., & Claret, A. 2002, A&A, 382, 1009
Wilson, R. E. 1979, ApJ, 234, 1054
Wilson, R. E., & Devinney, E. J. 1971, ApJ, 166, 605
Wolff, S. C., Strom, S. E., Dror, D., & Venn, K. 2007, AJ, 133, 1092